Chapter 11

Magnetic properties of 2D islands on single-crystal metal surfaces

H. Brune* **and S. Rusponi**

Institut de Physique des Nanostructures, Ecole Polytechnique Fédérale de Lausanne (EPFL), CH-1015 Lausanne, Switzerland

1. INTRODUCTION

Exploring the ultimate density limits of magnetic information storage, whether on computer hard disks or in MRAMs (magnetic random access memories), requires elaborate tuning of the preferred (easy) magnetization axis, of the magnetic anisotropy energy (MAE), and of the magnetic moment in the units used to store a bit. These units are single-domain particles (with diameter $d < 20\,\text{nm}$) where the magnetic moments of all atoms are ferromagnetically aligned [1] to form the overall magnetic moment of the particle **M**, also called the macrospin. The preferred orientations of **M**, and the anisotropy energy barriers $\boldsymbol{K}$ separating them, are given by the delicate balance between several competing energies. These are the magnetocrystalline bulk anisotropy, its surface and step counterparts, and the shape anisotropy or demagnetizing energy resulting from the interaction of **M** with its own dipolar stray field.

The resulting overall anisotropy energy defines the stability of the magnetization direction against thermal excitation, and therefore the minimum particle size for which non-volatile information storage may be achieved (at 300 K this requires $K = 1.2\,\text{eV}$). However, unraveling the origin of anisotropy is far from trivial due to the competition between these energies [2]. A further key parameter is the modulus of **M**: M defining not only the dipolar stray field used to read and write, but also mediating interactions between adjacent bits. These interactions are minimized for out-of-plane magnetization and therefore uniaxial out-of-plane systems are best suited to explore the ultimate density limit of magnetic recording [3, 4].

Current studies attempting to identify the origin of magnetic anisotropy, and the density limit with which one may ultimately place magnetic particles without appreciable interactions, mainly deal with two model systems. These are colloids or three-dimensional (3D) nanoparticles, and 2D nanostructures created by molecular-beam epitaxy at single-crystal surfaces. For colloidal particles, remarkable progress has been

The Chemical Physics of Solid Surfaces, Volume 12
ISSN: 1571-0785
DOI: 10.1016/S1571-0785(07)12011-3

*Corresponding author.
E-mail: harald.brune@epfl.ch

achieved in monodispersity [5], their self-assembly into 2D superlattices [6, 7], and in the accomplished anisotropy energies per constituent atom [8, 9].

Despite their promising properties for applications, 3D nanoparticles present several difficulties. Although the magnetic properties of a single particle can be addressed [10], it is almost impossible to study the morphology of the particle in conjunction with its magnetism. The particles frequently have a few atomic layers of oxide at their surface, which are not ferromagnetic [11]. This causes uncertainties in the morphology of the ferromagnetically ordered particle core. Owing to these difficulties, no general view on the origin of anisotropy in nanoparticles has yet evolved. The anisotropy has either been attributed mainly to the volume [12] or surface [10] contribution of the crystalline lattice, or to shape anisotropy caused by eccentricities of the magnetic core [11]. A second difficulty is the out-of-plane alignment of the easy magnetization axes in colloidal monolayers. An individual particle can have several easy magnetization axes. In addition, the deposited particles are randomly oriented and therefore their axes point into random directions [13]. However, every in-plane component of the magnetization leads to undesired dipolar interactions. Attempts of applying out-of-plane magnetic fields during deposition piles up the particles by dipolar interactions and thereby inhibits formation of ordered monolayers [8]. A third difficulty is coalescence between adjacent particles upon annealing. This equally leads to high blocking temperatures and is often difficult to discern from the desired coercivity increase in the individual particles by change of their crystalline structure [12].

2D nanostructures at surfaces are optimally suited to address the origin of anisotropy, and also to explore density limits of non-interacting magnetic units. The anisotropy imposed by the substrate makes them uniaxial, for example oriented out-of-plane. The size and spatial uniformity achieved by self-assembly techniques [14–16] are comparable to those of colloids. Under ultrahigh vacuum conditions, there is no oxide shell and all constituent atoms are ferromagnetically ordered. Thus, the particle morphology contributing to the magnetic signal is accessible at the atomic scale and can be related to the magnetic properties measured in situ with integrating techniques.

Inspired by these advantages, and by the technological relevance of the questions raised above, many fundamental studies have been carried out on the magnetic properties of 2D islands on single-crystal metal surfaces. These studies use epitaxial growth and are therefore complementary to studies depositing magnetic clusters from the gas phase [17]. For general overviews of magnetic nanostructures and their technical applications, we refer to Refs. [1, 18–20]. We focus here in particular on experiments which try to establish an atomic scale understanding of the contribution of the individual constituent atoms to the magnetic properties of the overall island. One of the key experimental techniques is scanning tunneling microscopy (STM), either used to characterize the morphology of the island ensemble or to infer magnetic information on individual islands using spin-polarized (SP) tips. Magnetic properties such as spin and orbital moments, as well as anisotropy energies, are inferred by established spatially integrating techniques, such as magneto-optical Kerr effect (MOKE) and X-ray magnetic circular dichroism (XMCD).

We begin our chapter with a discussion of the temperature-induced transition from the blocked to the superparamagnetic state, followed by disappearance of magnetic order once the islands Curie temperature is reached. The mechanism of thermally activated magnetization reversal is still a non-trivial issue due to the difficulty to

characterize the transition state of the island either by experiment or theory. We discuss examples of coherent rotation and domain-wall nucleation, as well as curling. Section 3 takes Co islands on Pt(1 1 1) as an example to show the different contribution of step vs. surface atoms to the magnetic anisotropy. This system also demonstrates the non-triviality of magnetization reversal as it shows a transition from coherent rotation for small and compact islands to domain-wall nucleation upon a critical diameter which is for ramified islands in the range of 150 Å. We discuss self-assembly of magnetic island superlattices in Section 4. In the same section, we discuss the magnetic properties of superlattices. The first example are Co double-layer islands on an Au(7 8 8) surface which presently is the highest density of uniaxial out-of-plane particles with no dipolar interactions and most homogeneous magnetic moments and anisotropies. However, its blocking temperature is with 50 K too small to become technically relevant. The second example is Co pillars realized by sequential deposition of Co and Au onto Au(1 1 1). This system can be grown such as to be blocked at 300 K, however, it suffers from dipolar interactions. The island shape favors in-plane magnetization, nevertheless the islands are out-of-plane magnetized due to the magnetocrystalline anisotropy imposed by the substrate. The substrate role is addressed in Section 5 for individual magnetic adatoms on alkali surfaces showing different degrees of hybridization and revealing the ground state electron configuration. The evolution of orbital moment and anisotropy energy as function of lateral coordination is addressed for Co adatoms and small islands on Pt(1 1 1). Section 6 is devoted to spin-polarized STM measurements reporting spin-polarized surface states on Gd islands on W(1 1 0), unusually high tunnel magneto-resistance values for Co/Pt(1 1 1)–Cr/W tip junctions, and contrast inversion for Co islands on Cu(1 1 1) and Cr-coated W tips. Finally, we summarize and give future perspectives in the conclusions.

2. MAGNETIZATION VS. TEMPERATURE

The temperature evolution of the magnetic moment $M(T)$ of a nanoparticle shows three distinct regimes whose boundaries are the Curie temperature T_C and the blocking temperature T_b. These temperatures are the macroscopic signature of two atomic interaction energies. The first is the exchange interaction J, which leads to a magnetic moment of the nanoparticle for ferromagnetic alignment of the spins of adjacent atoms. The second is the spin–orbit interaction inducing coupling of the electron spins to the crystal field. This gives rise to magnetocrystalline anisotropy leading to the everyday experience that magnets are magnetized along preferential directions (easy axes). Besides magnetocrystalline anisotropy, there are several other sources of anisotropy, for instance magnetostriction, shape, and surface anisotropy. The resulting overall anisotropy is referred to as MAE K.

Briefly, the magnitude of $M(T)$ is determined by the exchange energy and the atomic moments, while the direction of $M(T)$ is determined by the MAE. Typical orders of magnitude are 1–20 meV/atom for J and 0.1–1 meV/atom for K. With increasing temperature, T_b marks the boundary between the blocking region, where the MAE keeps the magnetization direction parallel to the easy axis, and the superparamagnetic region, in which the nanoparticle can continually reverse its magnetization direction due to thermal excitation. T_c marks the boundary between the superparamagnetic

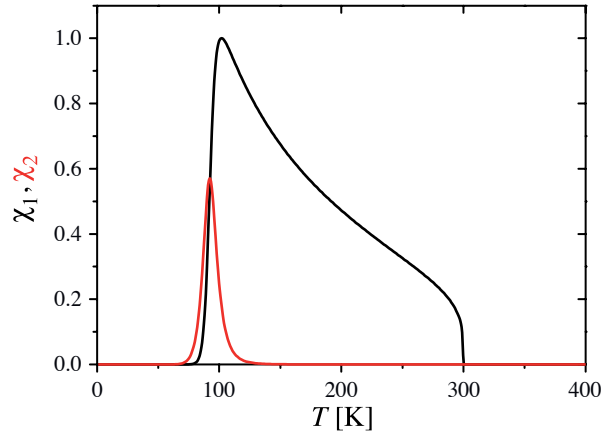

Figure 1: Temperature dependence of the zero-field susceptibility of a single particle. The black and gray curve represents the real and imaginary part of the susceptibility, respectively.

region and the paramagnetic region in which the thermal excitation breaks the parallel alignment of spins inside the particles.

This evolution is displayed by the temperature diagram of the zero-field susceptibility for a single-domain nanoparticle having a single easy magnetization axis (Fig. 1). Let us consider the nanoparticle in the blocked state with its magnetic moment aligned to the easy axis. In the absence of external magnetic field ($H = 0$), the spin *up* and spin *down* states are separated by an energy barrier $E(K)$ which is a function of the MAE K. Independently, on the details of the landscape shape of this energy barrier, the thermally activated magnetization reversal rate follows the Arrhenius law $\nu = \nu_0 \exp(-E/k_B T)$. The relaxation time τ is given by $\tau = \tau_0 \exp(E/k_B T)$, with $\tau_0 = \nu^{-1}$. The barrier is readily overcome if $T > T_b = E/k_B \ln(1/\omega\tau_0)$, where ω is related to the observation time $t = 2\pi/\omega$. In the case of Fig. 1, ω is the sweep frequency of the external magnetic field used to measure the susceptibility. T_b is the blocking temperature, defined by the temperature where the ensemble reaches half of its thermodynamic equilibrium susceptibility χ_{eq}. For $T > T_b$, the particles are superparamagnetic, and $\chi(T) = \chi_{eq}(T)$. For $T < T_b$, the particles are blocked in a fixed magnetization state (up or down), and hence $\chi(T) = 0$. For $T \approx T_b$, the system is determined by the kinetics of barrier crossing which depends on the actual shape of the energy barrier. Up to now, the overall magnetic moment $M(T)$ of the nanoparticle was assumed to be temperature independent which is equivalent to assuming an infinite Curie temperature. A more realistic description is obtained when introducing the temperature dependence of the magnetic moment in order to take into account that at $T = T_C$ the thermal energy overcomes the exchange energy causing the breaking of the ferromagnetic order in the island. For a uniaxial nanoparticle, a natural choice is given by the exact expression for the temperature dependence of the magnetization of a Ising lattice. For example, in the case of a plane triangular Ising lattice, it reads $M(T) = [(w(T)+1)^3/(w(T)-1)^3]^{1/8}[(w(T)-3)/(w(T)+3)]^{1/8}$, where $w(T) = \exp(4J/T)$ and $T_C = 4J/\ln 3$ [21]. This results in an abrupt drop of the real part of the susceptibility ($\chi_1(T)$) to zero at $T = T_C$ (Fig. 1).

It is instructive to move a step further in the understanding of the magnetization reversal problem. Three mechanisms are possible for the magnetization switching: coherent rotation, domain-wall nucleation with subsequent wall propagation, and curling. The thermal switching by coherent rotation was theoretically investigated by Neel [23] and Brown [24]. They assumed uniaxial MAE and single-domain magnetization, i.e., at any time during the reversal process the spin and orbital moments of the constituent atoms are ferromagnetically aligned to form a single magnetization vector, the nanoparticle macrospin $\boldsymbol{M}$. The energy diagram of this macrospin in an external magnetic field $\boldsymbol{H}$ is described by $E = K \sin^2 \theta - \boldsymbol{MH}$ with two minima, corresponding to the *up* and *down* orientation of $\boldsymbol{M}$, separated by the cluster's MAE K at zero field (θ is the angle between surface normal and $\boldsymbol{M}$). The anisotropy energy at zero field is the energy $K = E(90°)$, associated with the in-plane configuration forming the transition state that has to be overcome during magnetization reversal. The crossing rate of the MAE barrier is described, in the limit of small external field, by the Arrhenius expression $\nu = \nu_0 \exp((-K + HM)/k_B T)$ with $\nu_0 \sim 10^{10}\,\mathrm{s}^{-1}$ [22]. The temperature dependence of the switching field can also be calculated and it was experimentally measured by Wernsdorfer et al. [22] for individual ellipsoidal cobalt nanoparticles having a diameter of 25 ± 5 nm (Fig. 2).

The thermally activated magnetization reversal by domain-wall nucleation and displacement was theoretically investigated by Braun for the 1D problem, or equivalently for elongated particles (particles with an in-plane aspect ratio larger than 1:10) [26–28]. Braun demonstrated that the excitation (or nucleus) with the lowest energy is an untwisted domain-wall pair and once this nucleus has formed the magnetization can reverse without further expense in energy. The nucleation barrier is proportional to the particle vertical cross-section S_z and in the limit of small field ($H < 2K/M$) reads $E = 8S_z\sqrt{JK}$, where K includes contributions of crystalline and shape anisotropies. One defines a critical length L_{cr} by comparing the previous energy with the energy required for the coherent magnetization rotation, which, for a uniform MAE

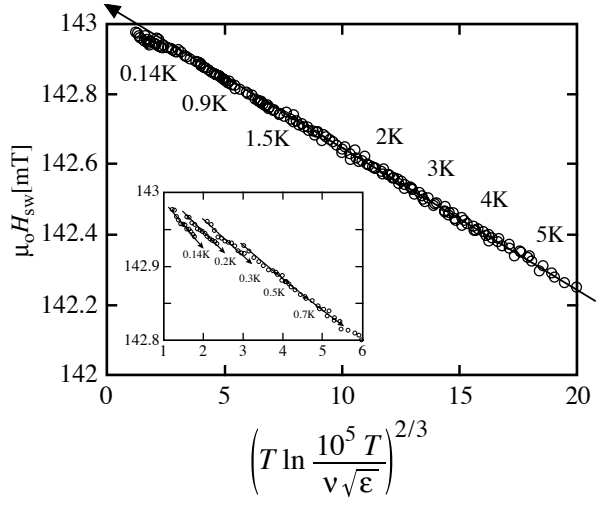

Figure 2: Scaling plot of the mean switching field H_{sw} for field sweeping rates between 0.01 and 120 mT/s and temperatures between 0.14 and 5.0 K. After Ref. [22].

distribution, reads $E = S_z L_{cr} K$, giving $L_{cr} = 8\sqrt{J/K}$. Actually, for very elongated particles $L \gg L_{cr}$, the particle ends behave independently and at finite temperature, due to the thermal fluctuations, magnetization reversal by nucleation of a reversed domain at one particle end becomes energetically favorable [29–31]. In this case, the nucleation barrier $E = 4S_z\sqrt{JK}$ is half the value calculated for the untwisted domain-wall pair case and the critical length reads $L_{cr} = 4\sqrt{J/K}$ and $L_{cr} \approx 5\sqrt{J/\mu_0 M^2}$ for the two limiting cases of $\mu_0 M^2 \ll K$ [29] and $\mu_0 M^2 \gg K$ [32], respectively.

Experimental evidence of a shape-dependent switching behavior has been reported for one monolayer thick perpendicularly magnetized Fe islands on Mo(1 1 0). Spin polarized-STM measurements (SP-STM) recording thermal switching rates of individual islands containing some hundreds atoms suggested that elongated particles (with a maximum aspect ratio of 1:4) switch faster than equally sized compact islands [25]. The authors report a critical length of $L_{cr} = 9.1 \pm 0.3$ nm (Fig. 3).

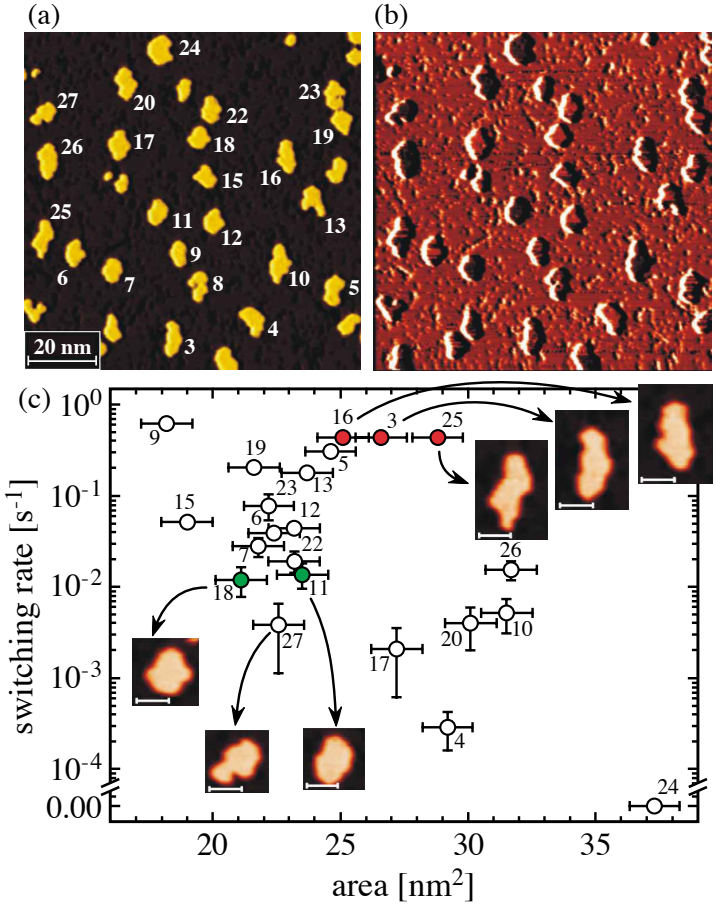

Figure 3: (a) Topography and (b) magnetic dI/dV signal of Fe islands on Mo(1 1 0). (c) Plot of the switching rate vs. the area of individual islands. The scatter of the switching rate points to a shape-dependent crossover from coherent rotation of compact Fe islands shorter than $L_{cr} \approx 9$ nm toward nucleation and expansion of reversed domains in elongated islands. (Insets) Topography of selected Fe islands (scale bar: 5 nm) [25].

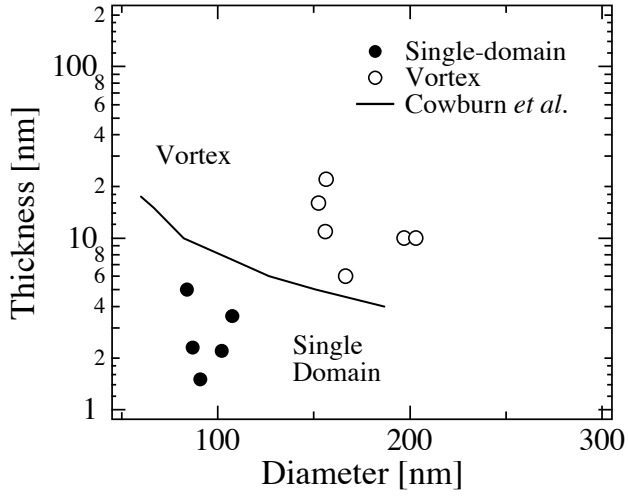

Figure 4: A phase diagram of magnetic states for different diameters and thicknesses of the Fe islands on W(0 0 1). Solid and open circles show the single domain and vortex state, respectively. The solid line is the dividing line following calculations by Cowburn et al. [33]. After Ref. [34].

Finally, the third reversal mode consists in the incoherent reversal by curling or vortex formation. This mode is in general unlikely in truly 2D nanostructures since the critical length for the turnover from coherent rotation to curling in an oblate spheroid quickly increases as the spheroid thickness is reduced [35]. For example, using bulk values for J and M, Skomski [36] evaluated a critical length of about 400 nm for a perpendicularly magnetized one monolayer thick Co film (one monolayer, ML, is defined as a coverage corresponding to the density of substrate surface atoms). Experimentally, SP-STM measurements of in-plane magnetized Fe islands on W(0 0 1) with a thickness of a few nanometers demonstrated that the single-domain state is stable for lateral sizes up to 200 nm [34] (Fig. 4).

3. Co ISLANDS ON Pt(1 1 1): MAE AND REVERSAL MECHANISM

In a 3D magnetic crystal, the magnetic anisotropy and the preferred directions of magnetization are related to the crystal axes by the quantum-mechanical spin–orbit interaction. As the dimension of a magnetic sample is reduced, for example in ultrathin (a few ML thick) films, e.g., used in the latest hard-disk read heads, the shape anisotropy caused by the magnetic stray fields outside the sample gains of importance. This anisotropy favors alignment of the magnetization along the film plane. Other energies that have their source in the electronic structure can be even more important. The reduced number of nearest neighbors of atoms at the surface of a thin film or at the edge of a nanostructure leads to more atomic-like electronic properties. 2D nanostructures created and analyzed under well-defined conditions (UHV, STM, and in situ magnetic characterization) represent an ideal prototype system to investigate the role of the different anisotropy energies, the reversal mechanism, and the contributions made by the differently coordinated constituent atoms.

3.1. Transition from blocking to superparamagnetic

With atomic beam epitaxy, several island morphologies can be produced by controlling the growth parameters [37]. The ramified islands in Fig. 5a are formed upon deposition at 130 K due to limited mobility of atoms along the island edge. Annealing of these islands to 300 K activates edge mobility yielding compact islands without much coarsening (see Fig. 5b). Further annealing to 340 K converts the monolayer-high islands of Fig. 5b into double-layer islands represented in Fig. 5c. This mutation is caused by the surface and interface free energies favoring atoms climbing up onto the second layer and thereby reducing, with respect to Pt(1 1 1)/vacuum, the more costly Co/vacuum and Co/Pt interfaces by a factor of 2.

The island size and perimeter distributions were obtained from a statistical ensemble of about 1000 islands imaged by STM for each sample. The size distributions are normalized to yield unit area under the curves. As expected, the size distribution of the ramified islands is very well reproduced by the theoretical curve obtained by kinetic Monte-Carlo simulations and by nucleation theory taking into account the random island spacing [38] (asymmetric bell curve, non-zero when $s \to 0$). The mean sizes for the three samples are: $S_r = 1000 \pm 600$, $S_c = 1200 \pm 700$, and $S_b = 5000 \pm 1500$ atoms. The nonlinear relationship between the island area and perimeter length (see insets) gives each of the two distributions its characteristic shape, thus enabling to disentangle the different role played by inner and edge atoms.

The magnetic behavior was characterized by measuring the temperature dependence of the zero-field susceptibility with MOKE. Independent of island shapes and sizes, a MOKE signal was observed only in polar configuration demonstrating an out-of-plane magnetization easy axis. The $\chi(T)$ curves were measured as the field derivative of the Kerr intensity with the external field sweeping around zero with frequency $\omega = 0.1$–$100\ \mathrm{s}^{-1}$ and an amplitude of 100 Oe. This amplitude is motivated by a trade-off between signal-to-noise and the linearity of the superparamagnetic $M(H)$ curves. In our case, they are linear up to much higher fields (linear response theory gives the upper field limit as $MH \ll k_B T$). All the $\chi_1(T)$ curves present the same characteristic behavior shown in Fig. 1.

We first consider fits of the experimental data assuming magnetization reversal by coherent rotation. MOKE is a spatially integrating method (the laser spot size was about $1\ \mathrm{mm}^2$) reporting the properties of the island ensemble. Accordingly, we sum over all islands, taking their size and perimeter distribution into account. The $\chi(T)$ function for a given island is obtained as follows. The kinetics of barrier crossing and therefore the residence time in the spin up and spin down states is described by master equations. In the limit of small fields one can linearize these equations and multiply with the equilibrium susceptibility to obtain the following analytical expression for the in-phase (real) and out-of-phase (imaginary) part of the zero-field susceptibility ($\chi = \chi_1 + i\chi_2$):

$$\chi_1(\omega, T) = \chi_{eq}(T) \frac{1}{1 + \omega^2 \tau^2} \tag{1}$$

$$\chi_2(\omega, T) = \chi_{eq}(T) \frac{\omega\tau}{1 + \omega^2 \tau^2} \tag{2}$$

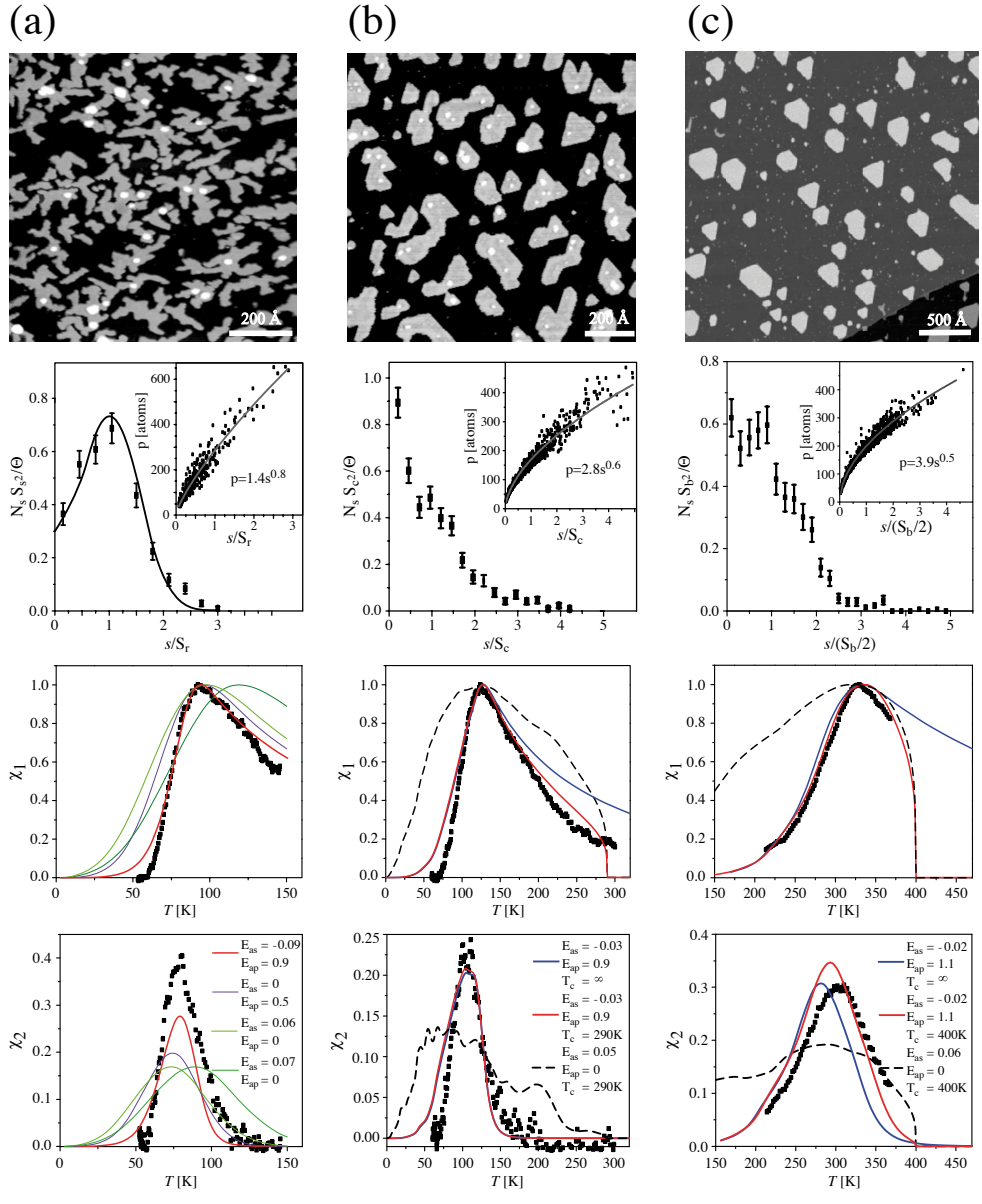

Figure 5: STM images, size s and perimeter p distributions, real ($\chi_1(T)$) and imaginary ($\chi_2(T)$) susceptibility curves for three different island shapes: ramified monolayer (column a), compact monolayer (column b), and bilayer (column c). S is the average island size, and N_s the density of islands of size s, the Co coverage is the same for the three morphologies ($\Theta = 0.4$ ML). In the size and perimeter distribution figures, the black and gray curves represent the best fits according to the text. In the susceptibility graphs, the various curves represent the fits according to the values for the MAE of inner (E^{as}) and edge atoms (E^{ap}) shown in the legends. The MAE values are given in meV/atom.

where $\tau = 1/v_0 \exp(K/k_B T)$ [39]. χ_{eq} is the zero-field susceptibility at thermodynamic equilibrium given by [40, 41]

$$\chi_{eq}(T) = M^2 \left[\frac{\exp(K/k_B T)}{\sqrt{\pi K k_B T}\,\mathrm{Erfi}(\sqrt{K/k_B T})} - \frac{1}{2K} \right] \tag{3}$$

This equation takes into account the fluctuations of the magnetization around the energy minima. The blocking temperature T_b is defined by $\omega\tau(T_b) = 1$. Its expression and the transition width are given by $T_b = K/k_B \ln(1/\omega\tau_0)$ and $\Delta T_b = k_B T_b^2/K \approx T_b/30$, respectively.

For $T < T_b$, the particle is blocked in a fixed magnetization state (*up* or *down*), hence $\chi(T) = 0$ (blocked region). For $T \approx T_b$, the crossing over the MAE barrier is thermally activated and the magnetic state of the particle is determined by the kinetics of barrier crossing (activation region). This is reflected in a peak both in the $\chi_1(T)$ and in the $\chi_2(T)$ curves. Finally, for $T > T_b$, the particle is superparamagnetic, and $\chi(T) = \chi_{eq} \propto 1/T$ (superparamagnetic region). For comparison, Fig. 6 shows the infinite anisotropy limit, leading to a two-state system (Ising model, see dashed short curves in main figure and inset), and the vanishing anisotropy limit, characterized by an occupation of all orientations of M (Langevin model, long dashed curves). With increasing temperature, χ_{eq} goes from one limit to the other and therefore its decay is slightly steeper than the $1/T$ behavior characterizing the two limiting cases. It is seen that the Ising model is a good approximation for $\chi(T)$ if $T_b < T < 2T_b$, whereas the Langevin model may only be used for very high temperatures.

The origin of M and K is revealed by testing different assumptions to compute these values for a given island with size s and perimeter p. In order to keep the fitting to a single parameter, we assume that M is simply given by the number of constituent atoms times their moment m, $M = sm$. This assumption is justified because m varies by much less than 20% for the size range of interest [42]. m was determined by measuring the magnetization curve of compact islands at $T > T_b$. Figure 7 shows the typical superparamagnetic reversible S-shaped curve. The magnetization reaches 0.6 of its saturation value at the experimentally available field of ± 500 Oe. With the Ising model, which is a good approximation just above T_b, we obtain the gray curve yielding $m = 2.1 \pm 0.2\,\mu_B$ per atom. This value is in very good agreement with the one expected from taking the sum of the calculated Co spin moment [43] $m_{Co,S} = 1.8\,\mu_B$, its measured orbital moment [44] $m_{Co,L} = 0.2\,\mu_B$, and the measured polarization of Pt at its interface with Co amounting to [45] $m_{Pt} = 0.2\,\mu_B$. We note that already for the moments the size distribution and obviously the correct models are crucial. Assuming an ensemble of particles all having the average size would give $m = 3.0 \pm 0.2\,\mu_B$ per atom and erroneously using the Langevin model would yield $m = 6 \pm 1\,\mu_B$ per atom. Note also that M respectively m enter as scaling factor on the vertical axis. This implies that the reference measurement on a fully saturated monolayer sample was essential to measure m, however, it also implies that errors on M do not affect the shape of $\chi(T)$ which is used to determine the MAE K. Conclusions reached below on K are independent of the exact value of m.

The MAE of a particle strongly depends on the coordination of the constituent atoms [16, 46–48]. Therefore, the natural choice for the expression of the MAE is $K = sE^{as} + pE^{ap}$, where E^{as} and E^{ap} are the contribution of highly coordinated (inner)

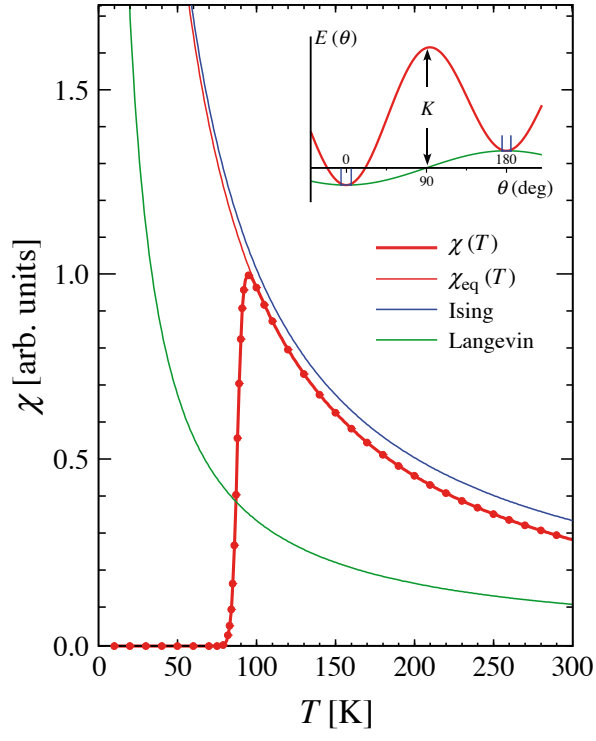

Figure 6: Zero-field magnetic susceptibility $\chi(T)$ for a magnetic island with out-of-plane easy axis. Different models are compared for $K = 200\,\text{meV}$, $M = 3150\,\mu_B = 182\,\text{meV/T}$ corresponding to islands with 1500 Co atoms triangular field sweep with $\omega = 0.3\,\text{Hz}$. The analytical model ($\chi(T)$, thick full curve) perfectly describes the blocking to superparamagnetic transition as seen by comparison with the numerical calculation (circles). The equilibrium zero-field susceptibility, χ_{eq}, is shown as a thin gray curve. (Inset) Energy of a uniaxial monodomain particle as a function of the orientation of M with respect to an out-of-plane external field H in the Ising model (two states: up and down), in the Langevin model (continuum of states, no anisotropy, E is given by Zeemann energy HM), and in the full model incorporating the anisotropy energy K. $\chi(T)$ derived from the Ising and Langevin models are shown in the main figure for comparison.

and low coordinated (edge) atoms, respectively. By simultaneously fitting the $\chi_1(T)$ and $\chi_2(T)$ curves the following magnetic anisotropy energies per atom are obtained for the three island morphologies:

- ramified: $E^{ap} = 0.9\,\text{meV}$, $E^{as} = -0.09\,\text{meV}$
- compact: $E^{ap} = 0.9\,\text{meV}$, $E^{as} = -0.03\,\text{meV}$
- bilayer: $E^{ap} = 1.0\,\text{meV}$, $E^{as} = -0.02\,\text{meV}$

with an error of $\pm 0.1\,\text{meV}$ ($\pm 0.2\,\text{meV}$ in the case of bilayer islands) on E^{ap} and $\pm 0.003\,\text{meV}$ on E^{as}.

The value $E^{ap} \approx 1\,\text{meV/atom}$ associated to edge atoms, having on average four in-plane neighbors, compares well with the MAE/atom measured by means of XMCD in small Co clusters on Pt(1 1 1) with a size of 7–10 atoms, where the lateral coordination

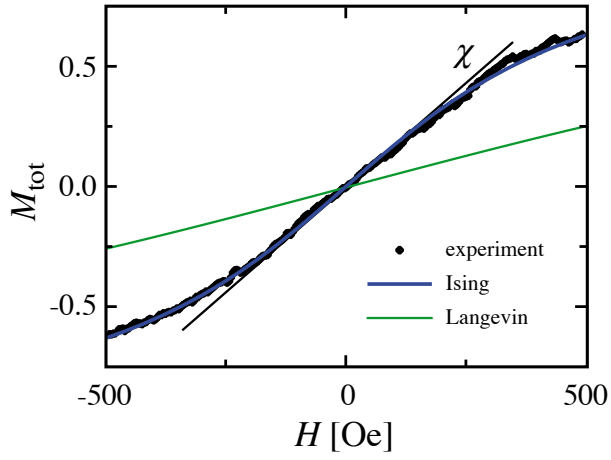

Figure 7: Magnetization (M_{tot}) of the sample shown in Fig. 5b as a function of out-of plane field. $T = 150$ K, triangular field sweep with $\omega = 0.6$ Hz. M_{tot} is normalized to the Kerr signal obtained for saturation of a single monolayer film, taking the coverage of 0.4 ML into account. The Ising fit is shown as a gray line and yields $m = 2.1\ \mu_B$ when taking the size distribution into account. The dash dotted line is the Langevin model with this value.

of the majority of the constituent atoms is comparable [46] (see Section 5). It is also in good agreement with the value of 0.8 ± 0.1 meV/atom observed for Co islands on Au(7 8 8) [16], and with the estimate of 1.0 ± 0.3 meV/atom derived from Ref. [48] for Co islands on Au(1 1 1). For the bilayer islands, this value seems high since the first layer perimeter atoms are higher coordinated and therefore expected to have lower anisotropy than the second layer step atoms. The larger error in the estimation is not due to deficiencies in the fit procedure but is due to the fact that nominally identical samples actually show different T_b. Possible causes are the different strain affecting border atoms in mono- and bi-layer islands [47] modifying the local density of states or different relaxation of the tensile stress taking place during the annealing procedure.

The predominant role played by the border atoms in determining the MAE is also directly pointed out by the shape of the $\chi_2(T)$ curves. An MAE proportional to the island size would result in a much broader $\chi_2(T)$ curve with respect to the measured one (Fig. 5). This directly follows from geometrical considerations since in 2D the island size has a distribution twice as wide as the one of the perimeter. By comparing with 3D colloid particles, where the MAE distribution is always larger than the one of the size [5, 11], this also means that arrays of 2D nanoparticles grown by MBE may achieve narrower MAE distribution than anticipated on the basis of the size distribution alone [16] (see Section 4).

The previous analysis was focused on the temperature range centered around the peak of the $\chi(T)$ curves containing the information about the MAE distribution of the samples. Nevertheless, it is instructive to get a closer look to the high-temperature region where a faster than predicted decrease of $\chi_1(T)$ is observed both for compact and bilayer islands. In the previous discussion, $M(T)$ was assumed to be temperature independent. Removing this assumption and assuming $M(T) = [(w(T)+1)^3/(w(T)-1)^3]^{1/8}[(w(T)-3)/(w(T)+3)]^{1/8}$, where $w(T) = \exp(T_C/T \ln 3)$, which is the exact expression for the temperature dependence of the magnetization of a plane

triangular Ising lattice [21], gives a better fit. In the case of compact islands, the fit gives $T_C = 290 \pm 10$ K. The absence of the abrupt drop of the susceptibility signal at $T = T_C$ can probably be ascribed to the island morphology. Some small second layer clusters in fact decorate the compact islands. Because T_C strongly depends on coordination, these second layer nuclei can locally increase the island T_C explaining the weak signal still visible around the estimated Curie temperature.

In the case of bilayer islands, the best fit gives $T_C = 400 \pm 10$ K. This value agrees with the following theoretical estimation. The Curie temperature of ultra-thin films is expected to depend on the film thickness n following the relationship [49] $1 - T_C(n)/T_C(\infty) = A - (n-1)/2N_0$, where N_0 is the range of spin–spin interaction and A is a constant taking into account the non-zero Curie temperature of the monolayer film (from the monolayer data one calculates $A = 0.79$). In the case of Co, the range of the spin–spin interactions has been calculated [50] to be $N_0 = 9$–10, which gives $T_C(2) = 370$–450 K. The experimental check of this value is difficult because annealing at temperatures slightly higher than about 380 K produces irreversible change of the $\chi(T)$ curves which tend to flatten while the island morphology stays unchanged. A similar onset temperature was recently measured by Robach et al. [51] who observed a 6 ML Co film on Pt(1 1 1) to reverse its magnetization from in-plane to out-of-plane following a brief annealing to about 375 K. By analyzing the magnetic crystal truncation rods of the Pt surface, the authors found the origin of the observed change of the film MAE in the site exchange between interfacial Co and Pt atoms. They also estimated the exchange to affect only $4 \pm 1\%$ of the interfacial Co monolayer. This interfacial exchange could be responsible for the evolution of the magnetism observed for annealing temperature higher than about 400 K. The partial Co/Pt exchange will likely produce a widening of the island MAE distribution which is seen as a widening and flattening of the $\chi(T)$ curves.

Before turning to alternative mechanisms of magnetization reversal, we briefly discuss the effect of mutual dipolar interactions. Looking at the agreement between experimental and calculated data for $\chi_1(T)$ in the superparamagnetic regime, showing the steeper than $1/T$ decrease, suggests absence of such interactions since their presence would considerably flatten this decrease [52]. The absence of interactions can be also rationalized by simply comparing the switching field H_{sw} of a given island with the stray field H_{stray} created by all other neighbors. The worst case is obtained assuming all the macrospins of the neighbors to be aligned. Considering an ensemble of monodisperse compact monolayer particles with $M = S_c \mu_{Co} = 146$ meV/T ($K \approx 120$ meV) one gets $\mu_0 H_{stray} \approx 1 \times 10^{-2}$ T (Eq. (4) of Ref. [53]). The temperature dependence of the switching field is given by $H_{sw} = H_0(1 - \sqrt{T/T_b})$ [54], where $\mu_0 H_0 = 2K/M = 1.6$ T. It is easily seen that dipolar interactions affect the islands behavior only when $0.99\, T_b < T < T_b$.

3.2. Magnetization reversal

The previous discussion assumed magnetization reversal by coherent rotation. However, Section 2 showed an example where 2D nanostructures reversed their magnetization by domain-wall nucleation. The size decides which of the two reversal processes is energetically favored. Magnetization reversal takes place by coherent rotation if the island diameter is smaller than L_{cr}, otherwise wall nucleation and subsequent motion costs less energy. In order to estimate the critical length for Co/Pt(1 1 1), we note that

the mean MAE value is $K \leqslant 0.15\,\text{meV/atom} = 1.5\,\text{MJ/m}^3$, assuming an identical contribution of all the atoms forming the islands [39]. This implies $K \geqslant \mu_0 M^2$ which is unfortunately just in-between the two limiting cases $\mu_0 M^2 \ll K$ and $\mu_0 M^2 \gg K$ which can be treated analytically. Evaluation of L_{cr} for the Co particles in the two cases gives 8 and 10 nm, respectively.

A more realistic evaluation of the critical length L_{cr} was obtained by performing micromagnetic calculations of the magnetization reversal process in absence of thermal excitation. The calculations employed the widely used OOMMF program which calculates the motion of the magnetization vector following the Landau–Lifshitz–Gilbert equation under the effect of a local field taking into account the exchange and dipole–dipole interaction, and uniaxial anisotropy energy [55]. We considered rectangular islands, however, rounding of the corners did not affect the results. The height (z) was set to 2.5 Å (1 ML) and the width (y) and length (x) were varied in order to see the effect of the island elongation on the magnetization reversal mechanism. The initial magnetization was assumed to be saturated ($m = 1.4\,\text{MA/m} \approx 2.1 \mu_B/\text{atom}$) and canted respect to z by an angle of $\theta = 182°$. This angle corresponds to the maximum possible misalignment between surface normal and magnetic field and allows convergence of the micromagnetic calculation with reduced magnetic fields ($\mu_0 H < 2K/M$) applied along z. The exchange stiffness was assumed to be $J = 10^{-11}\,\text{J/m} = 16\,\text{meV/atom}$ [56, 57] and $K = 0.15\,\text{meV/atom} = 1.5\,\text{MJ/m}^3$ following the experimental value.

In Fig. 8, the spatial distribution of the island magnetization is shown for different island dimensions. The snapshots are taken when the total z component of the magnetization $M_z = 0$. Clearly, the magnetization reversal proceeds by nucleation and displacement of an untwisted domain-wall pair for the longer islands, while the favorite mechanism is coherent rotation for the shorter ones, the critical length being $L_{cr} \geqslant 30\,\text{nm}$. The micromagnetic calculations also extend the validity limits of the

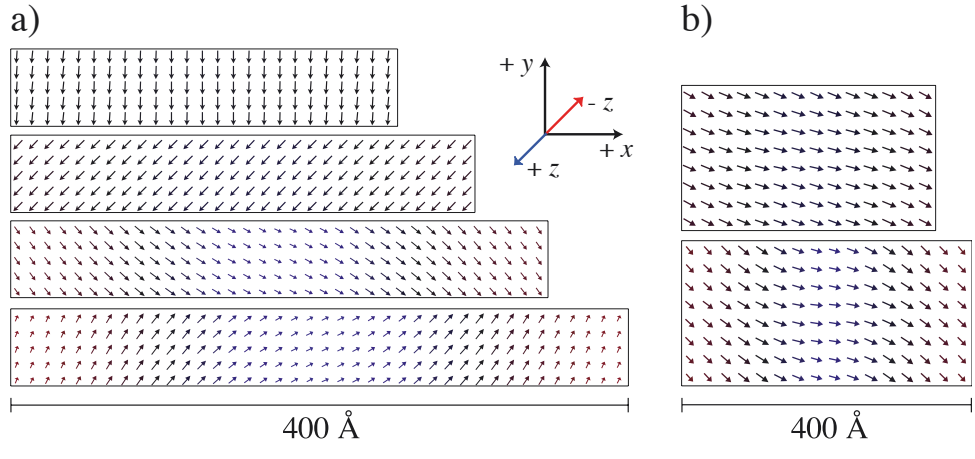

Figure 8: Micromagnetic calculations of the island magnetization. The snapshots show the magnetization distribution corresponding to a vanishing value of the total z-component of the magnetization ($M_z = 0$, $J = 10^{-11}\,\text{J/m} = 16\,\text{meV/atom}$, $m \approx 1.4\,\text{MA/m} \approx 2.1\,\mu_B/\text{atom}$, $K = 0.15\,\text{meV/atom} = 1.5\,\text{MJ/m}^3$). The MAE is assumed uniaxial along z. The damping coefficient was $\alpha = 0.1$ and the vertical field was $B_Z = 0.9\,\text{T}$. The islands were discretized by cuboids with a lateral size of 2.5 Å. The island height was set to 2.5 Å. The width (y) was fixed to 50 Å (a) and 200 Å (b).

analytical theory by supporting the independence of L_{cr} on the island aspect ratio (Fig. 8). This means that the magnetization reversal proceeds by wall nucleation and displacement as soon as at least one of the in-plane island dimensions becomes longer than L_{cr}. We note that the critical length strongly depends on the exchange stiffness which in turn depends on the island thickness. The value used in the simulations was measured for an 8 ML thick film, and it could be smaller for 1 ML [25, 57]. For example, one gets $L_{cr} \geqslant 20$nm nm for $J = 5 \times 10^{-12}$ J/m = 8 meV/atom. By assuming the energy barrier for nucleation at the particle end being half the one required for nucleation in the particle center, the micromagnetic simulations roughly estimated $L_{cr} \geqslant 15$nm. Considering for example the sample in Fig. 5b, the islands have lengths smaller than 20 nm with only a minor fraction having lengths up to 30 nm.This suggests that reversal by coherent rotation of the magnetization is a good approximation and that, eventually, only a negligible fraction of the islands may reverse their magnetization by domain-wall nucleation and displacement. Evidently, all simulations and analytical models of this discussion assume a homogeneous distribution of K, and the experimental [46, 58] and theoretical [47] evidence of a significant increase of K with reduced coordination is not taken into account.

As a parallel check we note that the energy barrier for nucleation of domain walls may be assumed proportional to the island section. A rough estimation of the distribution of island sections is given by the distribution of the area-to-perimeter ratios. By fitting the $\chi(T)$ curves assuming the energy barrier for switching $E = s/p\ E_{sec}$, where $E_{sec} \propto 4\sqrt{JK}$, instead of $K = sE^{as} + pE^{ap}$, gives in general a slightly worse agreement with the experimental data, with the exception of the ramified islands (Fig. 9).

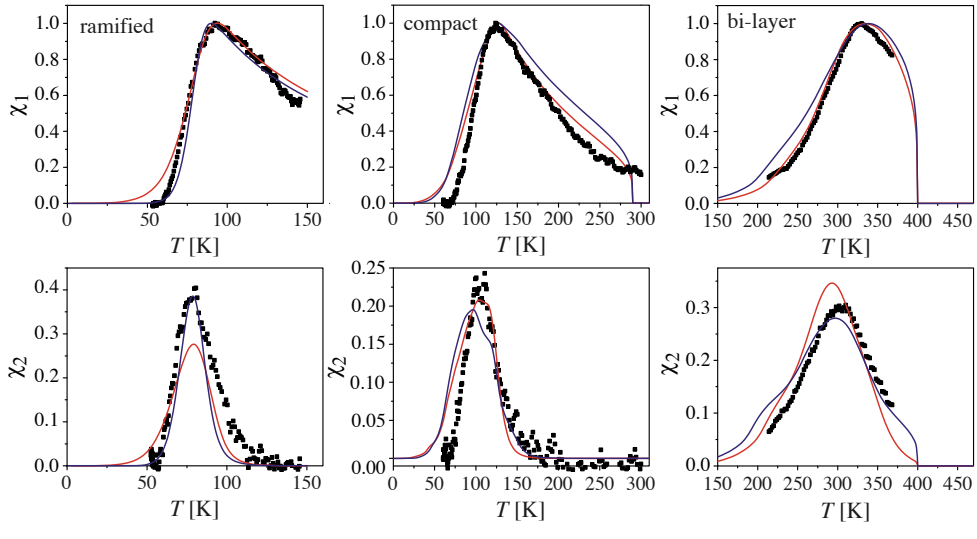

Figure 9: The experimental $\chi_1(T)$ and $\chi_2(T)$ curves measured for the three island shapes (ramified monolayer, compact monolayer, and bilayer) shown in Fig. 5. The black and gray curves represent the best fits assuming $E = s/p\ E_{sec}$ and $K = sE^{as} + pE^{ap}$, respectively.

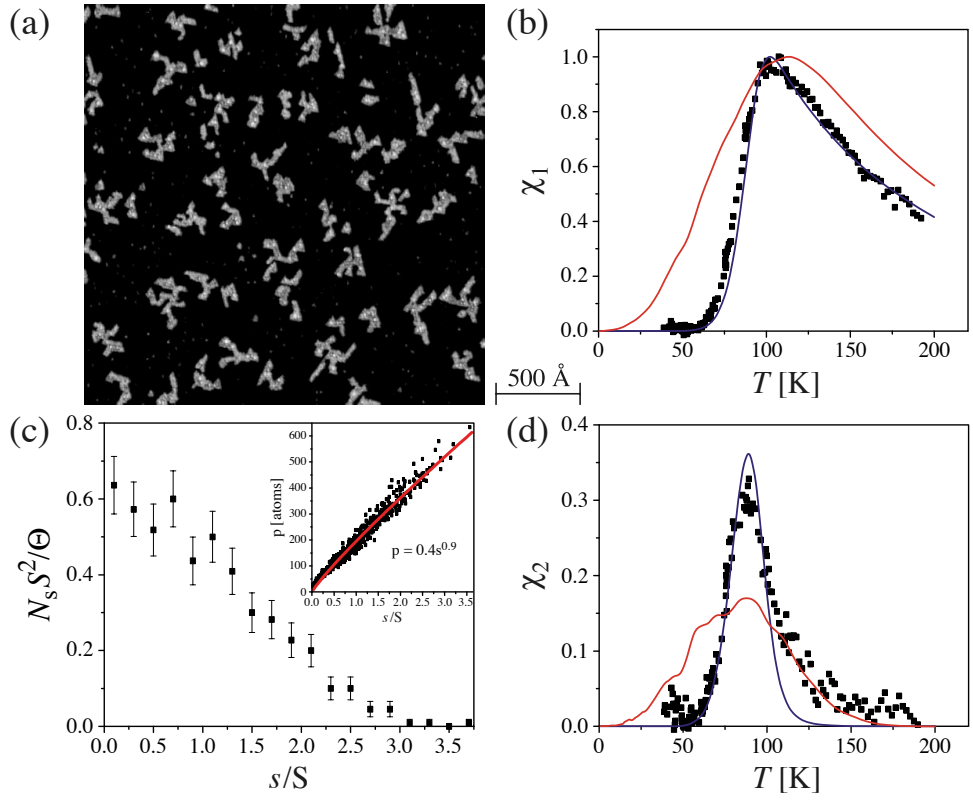

Figure 10: (a) STM image, (c) size s and perimeter p distribution, (b) real $\chi_1(T)$, and (d) imaginary $\chi_2(T)$ susceptibility for Co islands purposely grown to have a mean lateral size longer than 150 Å. The mean size is $S = 1100 \pm 800$ atoms. The black and gray curves represent the best fits assuming $E = s/p\ E_{sec}$ and $K = sE^{as} + pE^{ap}$, respectively ($\Theta = 0.08$ ML, $T_{dep} = 150$ K, subsequent addition of $\Theta = 0.08$ ML at $T_{dep} = 250$K).

To test where a transition to domain-wall nucleation possibly takes place for Co/Pt(1 1 1), we purposely chose growth conditions increasing the island length ($L \geqslant 15$ nm). Figure 10 shows that for this morphology a model assuming domain nucleation and motion nicely reproduces the experimental data points, whereas the fit assuming $K = sE^{as} + pE^{ap}$ gives an erroneous temperature dependence of $\chi(T)$. The proportionality constant in $E_{sec} \propto 4\sqrt{JK}$, which depends on the actual island shape, can be roughly estimated by comparing the values of the island mean section and of the ratio s/p measured by STM on a set of islands. By doing so and taking the fit value of E_{sec} one estimates $JK = 2.0 \pm 0.5\,\text{meV}^2/\text{atom}^2$, in good agreement with the value $JK = 2.4\,\text{meV}^2/\text{atom}^2$ assumed in the previous discussion. Altogether, this strongly suggests a transition from coherent rotation to domain-wall nucleation and motion for Co/Pt(1 1 1) at a critical length of $L_{cr} \approx 15$ nm.

3.3. Tailoring the magnetism of 2D nanoparticles

The finding of different contributions of step and surface atoms to the magnetic anisotropy opens new possibilities to separately tune the MAE and magnetic moment of

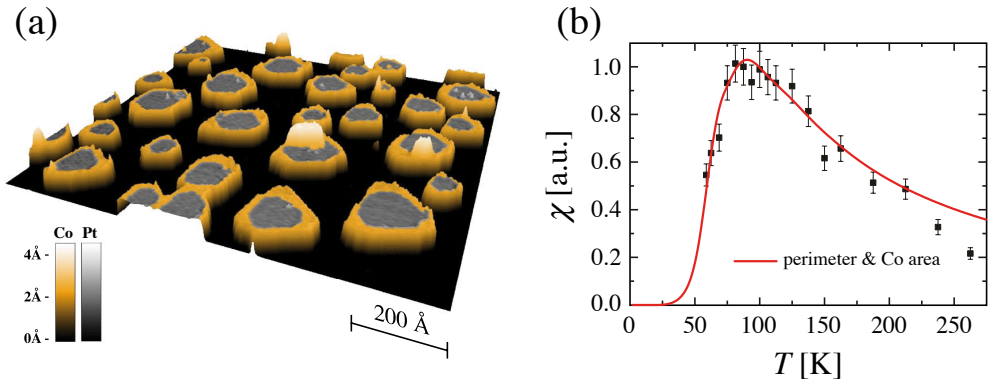

Figure 11: Tailoring magnetic properties in bi-metallic islands: (a) 3D view of an STM image of one monolayer high islands with Pt core and an approximately 3 atom wide Co shell (deposition of 0.2 ML Pt at 130 K and annealing to 760 K generates the quasi hexagonal non-magnetic core; subsequent deposition of 0.2 ML Co at 220 K creates the Co rim). In the STM topographs, Co can be discerned from Pt by its 0.3 Å larger apparent height which was used as color code; (b) $\chi(T)$ reveals that the Co-rim Pt-core islands have the same anisotropy as the pure Co islands with equal perimeter length [39].

nanostructures. The idea was exemplified by producing bi-metallic one monolayer high islands with a non-magnetic core (Pt), surrounded by a few atoms-wide magnetic rim (Co) (see Fig. 11a). The growth conditions took care that the rim is at least two atoms wide in order to increase the exchange-coupling energy and thus enforce long-range ferromagnetic order. In monatomic Co chains, where the chain atoms have only two magnetic neighbors, ferromagnetic order has been reported to extend only over 15 atoms at 45 K [59]. It is seen from Fig. 11b that keeping the MAE per edge atom fixed to the value inferred above for the pure Co islands perfectly reproduces the switching behavior. The bi-metallic islands have identical anisotropy as their equally shaped pure Co counterparts; however, they have a much smaller over-all moment due to their non-magnetic core, and thus reduced dipolar interactions. Many other examples where coordination and interfaces are employed to tailor K and M are currently under investigation.

3.4. Oxidation effect on the island MAE

Due to their reduced dimensions, small magnetic particles created by metal epitaxy at surfaces are very sensitive to pollution, in particular to oxidation. The effect of oxidation on the magnetic properties can be quite complex. Since oxidation generally starts at the low coordinated sites, partial oxidation may provide helpful insight into the origin of magnetic properties, such as magnetic anisotropy. Generally, oxidation degrades the magnetic properties, for instance it has been reported to reduce the anisotropy [60]. However, in particular systems it may dramatically increase the anisotropy, e.g., due to exchange coupling with an antiferromagnetic CoO shell [61]. STM images show clearly that the oxidation process begins at the island edge for Co/Pt(1 1 1) (Fig. 12). With increasing oxygen exposure, the dislocation pattern characteristic of clean Co is progressively replaced by a superstructure with a periodicity of 10 ± 1 Å. An oxygen dose of only 0.3 Langmuir is sufficient for the superstructure to cover the entire surface of small islands, whereas clean Co patches remain only in the center of the largest islands (Fig. 12c).

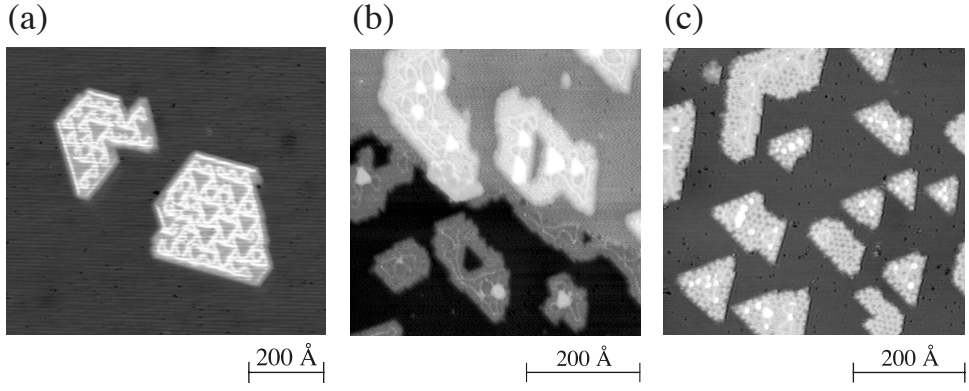

Figure 12: (a) STM image of one monolayer high pure cobalt islands on Pt(1 1 1) showing a triangular pattern of partial surface dislocations appearing bright and marking Co atoms adsorbed on bridge sites. (b) STM image of Co islands after the exposure to 0.05 Langmuir (L) O_2 showing selective oxygen adsorption starting at the steps removing the partials. (c) STM image of Co islands after exposure to 0.3 Langmuir of O_2. Only a small fraction of the larger islands have still the native strain relief pattern in their center, the remaining Co covered surface is transformed into an oxygen-induced 3×3 structure [58].

MOKE measurements show that partial oxidation modifies the temperature dependence of $\chi(T)$ in two ways. The temperature at which the maximum occurs is reduced, and the maximum taken on by $\chi_1(T)$ increases (Fig. 13a). This apparently strange effect can be understood with the help of a qualitative argument. The island MAE K strongly depends on the perimeter atoms. Thus, for a very small amount of oxygen, for which only the island edge is oxygen covered due to the selective adsorption at step sites [62], the anisotropy strongly drops. The island magnetic moment is less sensitive to oxidation and decreases proportionally to the oxidized fraction of the island. As can be seen from Fig. 13, this model also holds quantitatively [58]. It also explains the oxygen-induced compression of the MAE distribution reflected by the observed compression of the $\chi_2(T)$ curves.

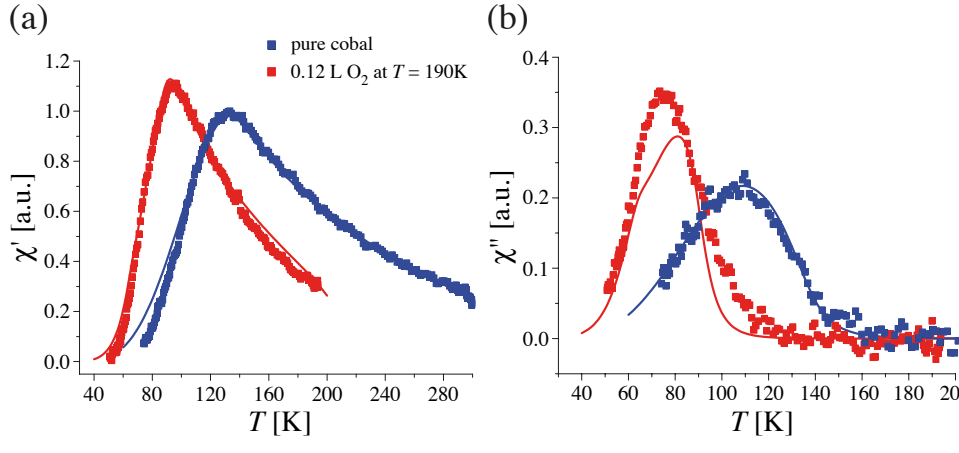

Figure 13: In-phase zero-field susceptibility (a) and out-of-phase zero-field susceptibility (b) as a function of temperature for pure and oxidized cobalt islands [58].

4. SUPERLATTICES OF UNIAXIAL MONODOMAIN ISLANDS

The bit density on magnetic hard disks has been increasing at a constant pace for many years [4]. This development creates technological challenges, such as reliable reading and writing of the bits; however, it also prompts the question after the fundamental ultimate density limit of magnetic recording. This question can be addressed by studying model systems consisting of periodically arranged ferromagnetic monodomain particles each of them potentially storing one bit. Ideally, the particles should have out-of-plane magnetic anisotropy since this minimizes mutual dipolar interactions. In order to achieve the required uniform write fields and read signals, the particles have to be uniaxial and the distributions of moments M and magnetic anisotropy energies K have to be narrow.

Several approaches have been used for the creation of such model systems. Examples are 2D superlattices of size-uniform 3D nanoparticles produced by colloidal chemistry or by precipitation [63], uniform shells with well-aligned easy magnetization axes [64] were produced by deposition onto superlattices of polystyrene particles, and self-assembly of equidistant 2D islands during atomic vapor epitaxy onto single-crystal template surfaces has led to the most uniform magnetic properties at the highest densities [16]. However, none of these approaches has so far led to the desired model system. The 3D nanoparticles will be a very promising material, once uniaxial particles with aligned out-of-plane easy axes can be achieved. The approach based on colloid lithography [65] has to be extended to smaller sizes, and self-assembly onto template surfaces has to be extended to bi-metallic and slightly larger particles in order to achieve blocking temperatures above 300 K. In the following, we present the results so far achieved with the latter approach.

4.1. Self-assembly of equidistant islands

The stress resulting from lattice mismatch in heteroepitaxial systems, and from missing bonds of the surface atoms often leads to weakly incommensurate surface layers. On close-packed surfaces, these layers have surface partial dislocations (domain walls) marking transitions between fcc- and hcp-stacking domains. These dislocations can be well localized, or extend over many lattice sites giving rise to smooth stacking transitions as in moiré patterns. The dislocations order into regular patterns due to the long-range repulsive interactions which for metals are mediated by elastic deformations extending far into the substrate. The density of dislocations is given by the achieved strain relief and can be adjusted in heteroepitaxial systems by the misfit between film and substrate elements. Examples for periodic dislocation patterns are the herringbone ($\sqrt{3} \times 22$) reconstruction of Au(1 1 1) [66], moiré patterns [67], or dislocation networks [68, 69] observed for metallic multilayers. For many systems, the surface partial dislocations represent strongly repulsive line defects for diffusing adatoms [70–72]. Their influence on nucleation can go as far as to drive the most perfect layer-by-layer growth yet observed [73]. However, they can also create sites with preferential incorporation of the deposited species [74]. Independent of the exact mechanism, the combination of ordered dislocations and their strong influence on adatom diffusion can often be employed to grow periodic arrays of almost monodisperse islands [37].

Concerning the magnetic properties of such superlattices, the most studied system is Co on Au(1 1 1) [42, 48, 75, 76]. We therefore discuss first nucleation at the elbows of

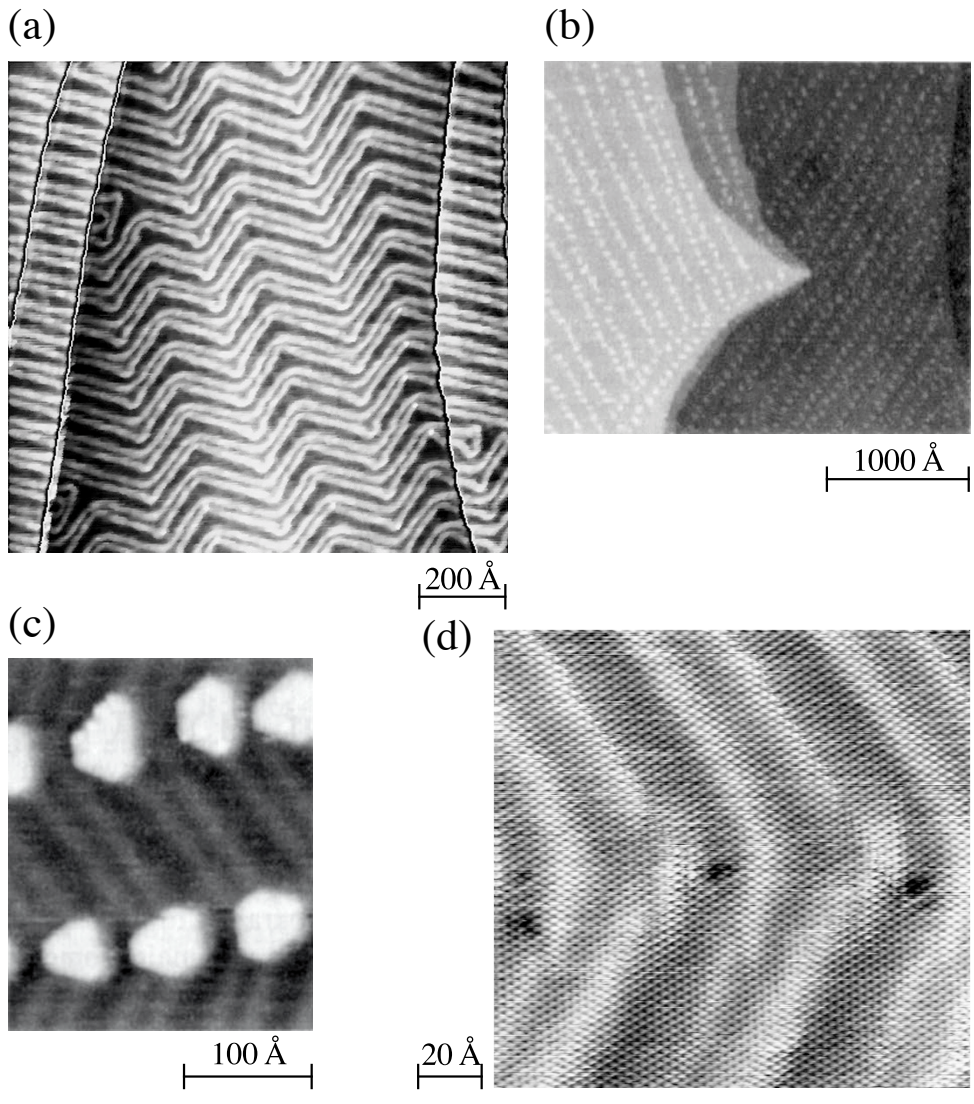

Figure 14: (a) STM image of the herringbone pattern characterizing the mesoscopic order of the Au(1 1 1)–($\sqrt{3} \times 22$) reconstruction [66]. (b) Ni nucleation on that surface at room temperature takes place at the elbows of the reconstruction ($\theta = 0.11$ ML) leading to Ni islands aligned in rows along the $\langle 1\ 1\ \bar{2} \rangle$-directions. (c) $\theta = 0.14$ ML [77]. (d) Site-selective incorporation of Ni into the first Au monolayer is revealed by deposition at 350 K giving access to the embedded Ni islands ($\theta = 0.002$ ML) [74].

the Au(1 1 1)–($\sqrt{3} \times 22$) reconstruction. Figure 14a shows the clean Au(1 1 1) surface with the $\langle 1\ 1\ \bar{2} \rangle$-oriented partial dislocations which are imaged 0.20 Å higher than fcc-areas and therefore appear bright. Stress relief is unidirectional in the ($\sqrt{3} \times 22$) unit cell. Along $\langle 1\ \bar{1}\ 0 \rangle$ there are 23 surface atoms on 22 bulk atoms, corresponding to a 4.3% compression, while the atomic distances remain the bulk value along $\langle 1\ 1\ \bar{2} \rangle$. To achieve overall isotropic surface stress, a well-ordered mesoscopic pattern of two domains with alternating orientation of $\pm 120°$ evolves on large terraces. Deposition

of Ni at room temperature leads to monolayer high Ni islands lined up along the elbows of the herringbone reconstruction pattern (Fig. 14b and c).

Ordered nucleation was initially believed to be caused by diffusing Ni adatoms being attracted toward the dislocation elbows by a higher binding energy there [77]. Due to the present knowledge, however, order results from site-selective exchange of Ni atoms with Au surface atoms [74]. The exchange is localized at the elbows where a close-packed atomic row terminates, giving rise to Au atoms with reduced lateral coordination which are especially susceptible to exchange or incorporation processes. The embedded Ni clusters, comprising four to five atoms each, are clearly detected as depressions in Fig. 14d. The site-selective exchange is followed by preferential nucleation of Ni adislands on top of substitutional Ni islands. Very similar order has also been found for Co [78, 79], Fe [80, 81], and Rh [82]. The mechanism is believed for all these systems to be identical to the one of Ni. The argument given by Meyer et al. is that the elements Ni, Co, Fe, and Rh have a larger surface free energy and heat of sublimation than Au [74]. In line with this argument, ordering is absent for elements with lower values of these quantities such as Ag [83] and Al [72]. However, Al/Au(1 1 1) exhibits exchange at $T > 245$ K [84, 85], showing the limits of this prediction solely based on bulk quantities.

Ordering by site-selective exchange is specific to Au(1 1 1) and related vicinal surfaces, and to elements of the periodic table exhibiting exchange on these surfaces. A more general approach relying on pure adatom diffusion on dislocation networks has been suggested [14]. Dislocations may confine adatoms by their repulsion to the unit cell into which they are deposited leading to the nucleation of exactly one island per unit cell. The repulsion of adatoms extends over some lattice sites avoiding nucleation close to the dislocation which would result in their overgrowth and create bridges between neighboring cells. In addition, fcc- and hcp-domains often have different adatom binding energies leading to one preferential nucleation site within each unit cell. Therefore, the potential energy surface seen by the diffusing adatom has a global minimum per supercell from which it goes smoothly upwards toward the edges. A similar distribution of binding energies may be realized on moiré patterns, one recent example being Ir/graphene/Ir(1 1 1) [86].

For ideal confinement, the size distribution is determined by the statistics of deposition into the unit cells. The probability of finding k atoms deposited within a unit cell with a size of n substrate lattice sites is a binomial distribution $P(k) = \binom{n}{k} p^k q^{n-k}$. This distribution has a standard deviation of $\sigma = \sqrt{q/np}$, where $p = \theta$ denotes the coverage in ML units, and $q = 1-p$. For Ag nucleation on 2MLAg/Pt(1 1 1)–(25 × 25), the measured size distribution was with $\sigma = 0.20$ wider than $\sigma = 0.12$ expected for ideal confinement at the coverage $p = 0.10$ and cell size $n = 625$ [14, 87]. Under ideal conditions, size distributions as narrow as $\sigma = 0.04$ are expected ($\theta = 0.50$, $n = 625$) but await experimental confirmation.

For magnetic elements, one often finds exchange or incorporation at random sites destroying order and therefore requiring careful choice of the template. While Co and Fe did exchange down to 50 K on 2MLAg/Pt(1 1 1)–(25 × 25), a template consisting of 2MLCu/Pt(1 1 1)–(13 × 13) [89] enabled the growth of ordered arrays of triangular monolayer high Fe and Co islands (see Fig. 15). Cu(1 1 1) is unstable upon exchange with Co down to 170 K [90], therefore low deposition temperatures had to be used. This led to the formation of three small clusters per unit cell which were subsequently

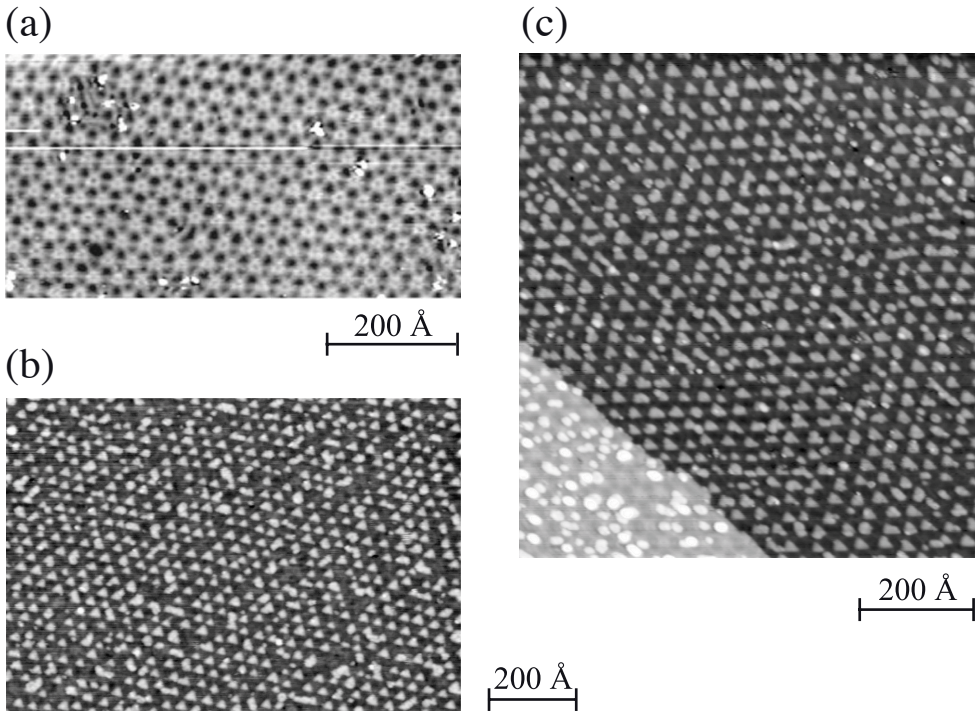

Figure 15: (a) STM image of the (13 × 13) dislocation network of 2 ML Cu on Pt(1 1 1) [88]. (b) Periodic arrangement of trigonal monolayer Fe islands formed by deposition at $T_{dep} = 100$ K and annealing at $T_{ann} = 250$ K onto the surface shown in (a) ($\theta = 0.10$ ML) [14, 88]. (c) Triangular Co islands obtained on 2MLCu/Pt(1 1 1)–(13 × 13) ($\theta = 0.10$ ML, $T_{dep} = 90$ K, $T_{ann} = 200$ K) [88].

transferred by gentle annealing into a single triangular island. From the surface free energies, Cu tends to cover Co and also Fe. Very different degrees of intermixing have been reported for Co/Cu(1 1 1). Early studies report etching of Cu for room temperature deposition of Co [91] and coexistence of both elements in islands [92]. Embedding of 3 ML high Co islands by one layer into Cu(1 1 1) upon deposition at 150 K [90], and entire capping of Co with Cu upon annealing to only 300 K have been reported [90, 93]. More recent studies investigating the electronic structure and therefore being very sensitive to intermixing are contradictory on the degree of intermixing. Pure Co adlayer islands for deposition at 290 K and subsequent rapid cooling, and intermixing upon deposition at 345 K are reported [94], while Co islands created at 300 K are reported to be surrounded by a few atoms wide Cu seam, independent of the speed with which the sample is quenched to low T [95]. Therefore, it is not excluded that a small fraction of the islands shown in Fig. 15 consists of Cu, even though the STM images show no direct evidence of this.

The preceding examples use templates exhibiting phase shifts between subsequent terraces. The last example uses Au(1 1 1) vicinal surfaces and thereby enables phase-coherent lattices over the entire crystal since atomic steps are used as nucleation sites. For appropriate orientation of the miscut, these surfaces exhibit energetically stable B-steps ({1 1 1}-microfacets) which, for not too small miscuts, are equidistant over the entire crystal due to elastic repulsions [96]. The (1 1 1)-oriented terraces exhibit the

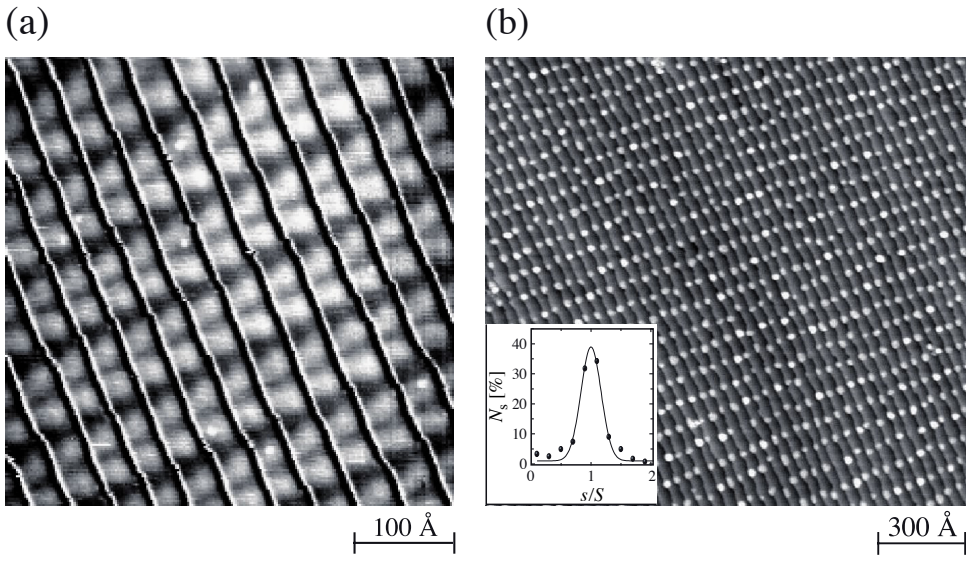

Figure 16: (a) STM image of the Au(7 8 8) surface. The corrugation due to the terrace levels has been subtracted in order to enhance the reconstruction lines [97]. (b) STM image showing 0.2 ML Co deposited on Au(7 8 8) at 130 K and annealed to 300 K. Co forms bilayer islands organized into a phase-coherent superlattice with a unit cell of 3.5 nm × 7.0 nm, corresponding to a density of 26 Tera-islands/in.^{2} (Inset) Size distribution with mean island size $S = 70$ atoms and $\mathrm{HWHM}_s = 14$ atoms; N_s denotes the abundance of islands with size s [16].

($\sqrt{3} \times 22$) reconstruction with domain walls running perpendicular to the step edges and being aligned from terrace to terrace (see Fig. 16a for the case of Au(7 8 8)).

Nucleation of Co takes place at the crossing of the domain walls and the steps [96, 97]. Figure 16b shows a typical pattern of double-layer Co islands obtained by depositing $\theta = 0.2$ ML Co onto Au(7 8 8) at 130 K and subsequent annealing to 300 K. This two-step process significantly increases the degree of order [96] with respect to direct deposition at 300 K [97]. The island size distribution in the inset of Fig. 16 is well reproduced by a Gaussian fit with $\sigma = 20\%$ which is close to the best value obtained for colloid particles. Comparing the Arrhenius representation of the island density with kinetic Monte-Carlo simulations including traps and exchange (insertion) yielded perfect agreement between simulation and experiment for trap energy $E_{\mathrm{trap}} = 0.28$ eV and a barrier for insertion $E_{\mathrm{ins}} = 0.78$ eV, compared with a diffusion barrier of $E_{\mathrm{m}} = 0.120 \pm 0.002$ eV [98].

However, Au vicinal surfaces present difficulties in growing bi-metallic islands due to exchange and incorporation. The ideal template, with a period of 50–100 Å, inducing magnetocrystalline out-of-plane anisotropy, and enabling annealing of the magnetic islands without intermixing, has yet to be discovered. We close by noting a few other templates which might be worse further investigation [99]. Moiré structures [100, 101] are quite promising since they can also be formed by thin sulfide [102], oxide [103], or nitride [104] films which are chemically more stable than metal surfaces. Very uniform cluster arrays were obtained for V [105] and Pd [106] on $Al_2O_3/Ni_3Al(1\,1\,1)$–($\sqrt{67} \times \sqrt{67}$)$R48^\circ$, while so far the clusters with magnetic elements, such as Fe, are less well ordered on this template [107]. While the lattice constant of the template is

normally a fixed number given by the misfit of overlayer and substrate, the lattice constant of 2D alloy layers is a function of their composition and generally given by Vegard's law. This enables growth of templates with adjustable supercell size, as has been shown for Au_xNi_{1-x} layers on Ni(1 1 1) [100]. Also, buffer layer assisted growth [108], where the metal atoms are evaporated onto an inert gas buffer which is subsequently desorbed, is a very promising approach since it enables formation of 3D clusters which may then land onto the surface. Monodisperse 3D clusters can be produced by combining cluster source with energy filter and mass selection [109]. These clusters can be soft-landed onto metal surfaces preventing fragmentation and/or incorporation into the substrate [110]. The latter two techniques produce size uniform but randomly spaced clusters. Uniform spacing may possibly be achieved by using these techniques on template surfaces.

4.2. Uniform magnetic properties of Co islands on Au(7 8 8)

The magnetic properties of the lattice shown in Fig. 16b were characterized by XMCD and MOKE. The spin (m_S) and orbital (m_L) moments of the Co atoms in the 2D islands have been determined by means of XMCD for a superlattice with a coverage of $\theta = 0.35$ ML, leading to a mean size of 120 atoms per island. Figure 17a shows the X-ray absorption spectroscopy (XAS) data for both helicities recorded under normal incidence at the Co $L_{2,3}$ absorption edges (2p to 3d transitions) and at a magnetic field of 5 T saturating the sample. From the resulting XMCD spectrum, m_S and m_L can be derived by means of the sum rules [111, 112]. The angular dependence of m_L is displayed in Fig. 17c and shows that the sample easy axis is within the error bars the

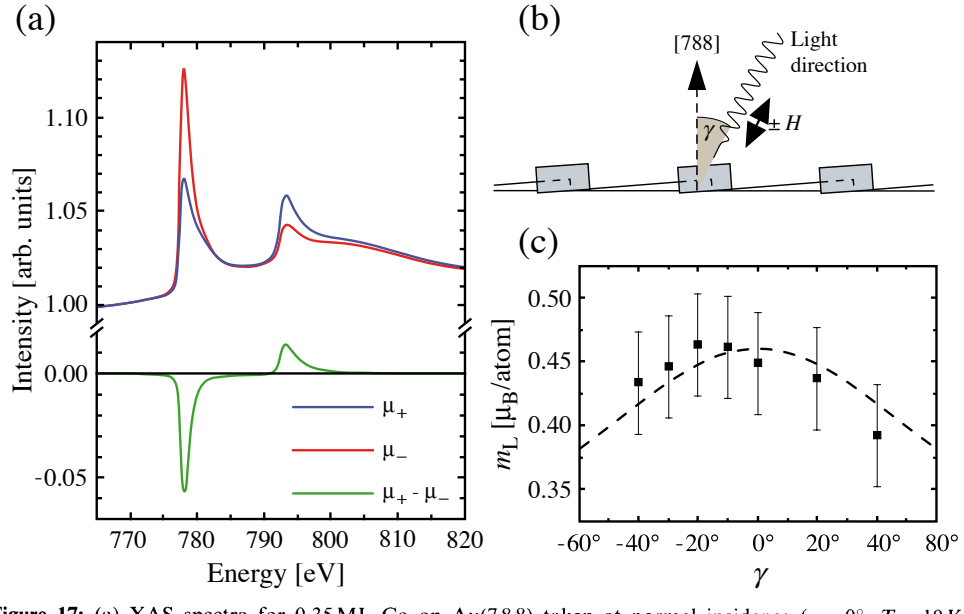

Figure 17: (a) XAS spectra for 0.35 ML Co on Au(7 8 8) taken at normal incidence ($\gamma = 0°$, $T = 10$ K, $B = 5$ T, $B_{sat} = 2.5$ T). μ_+ and μ_- are spectra recorded with left and right circularly polarized light, the difference is the XCMD signal. (b) Magnetic field and incident beam are parallel and form an angle γ with the surface normal. (c) Orbital moment m_L as a function of γ. The line corresponds to the fit with Eq. (4). After Ref. [16].

surface normal, in agreement with the results for Co islands on Au(1 1 1) [42, 48]. The data suggest a slightly canted easy axis since the highest m_L value is found at $\gamma \simeq -15°$. This is expected due to the fact that the Co islands are attached to substrate steps [113] which breaks the symmetry in the direction perpendicular to the steps. However, for simplicity and since the data do not provide significant support for a slight canting we assume the easy axis to be out-of-plane. The perpendicular and parallel component of the orbital moment, $m_{L,\perp}$ and $m_{L,\parallel}$, are therefore given by

$$m_L(\gamma) = m_{L,\perp} + (m_{L,\parallel} - m_{L,\perp})\sin^2(\gamma) \tag{4}$$

This gives $m_{L,\perp} = (0.46 \pm 0.05)\,\mu_B$ and $m_{L,\parallel} - m_{L,\perp} = (0.11 \pm 0.01)\,\mu_B$. Applying the sum rules and the formalism described in Refs. [111, 112, 114], a spin moment of $m_S = (1.7 \pm 0.1)\,\mu_B$ per Co atom was found, close to the bulk value [115]).

The MAE distribution of the Co islands was determined by considering a superlattice of slightly larger islands created by repeating the deposition and annealing sequence previously described in coverage steps of at most 0.3 ML. This procedure allows a linear increase of the island size preserving a narrow size distribution until the onset of coalescence ($\mathrm{HWHM}_s = 32\%$ for a coverage of $\theta = 0.75$ ML (see Figs. 18a and b). The zero-field susceptibility $\chi(T)$, shown in Fig. 18c, has a sharp peak at $T_b = 50$ K marking the transition from the blocked state to the superparamagnetic one. This transition takes place in a narrow temperature window of about 15 K, indicative of a very narrow MAE distribution. A fit with Eq. (1) taking into account the real size and perimeter length distributions, measured by analyzing the geometry of more than 2000 islands acquired by STM, and assuming $K = pE^{ap}$ and $M = sm_{Co}$ with $m_{Co} = m_L + m_S = 2.2\,\mu_B$ reproduces the experimental data very well with $E^{ap} = 0.8 \pm 0.1$ meV/atom.

A consistency check of the MOKE and XMCD measurements was done by comparing the islands MAE measured with both techniques. The mean island size of the sample studied with XMCD is $s = 120$ atoms, with $p = 55$ atoms situated at the rim. Therefore, $M = 264\,\mu_B$ and from MOKE $K = pE^{ap} = 44 \pm 5$ meV. The anisotropy of m_L, measured by XMCD, is linked to the magnetocrystalline anisotropy energy per atom, E_{MC}, by [42, 116–118]

$$E_{MC} = -\alpha \frac{\xi}{4\mu_B}(m_{L,||} - m_{L,\perp}) \tag{5}$$

with $\xi = 70$ meV, the Co spin–orbit coupling constant [42], and α accounting for the fact that the exchange splitting is generally smaller than the width of the band [114, 118]. Since MOKE determines the total anisotropy $K = E_{MC} + E_{shape}$, the shape anisotropy has to be subtracted. Assuming circular island geometry one estimates $E_{shape} = -0.08$ meV/atom, favoring in-plane magnetization, which yields an MOKE value of $E_{MC} = 0.45 \pm 0.04$ meV/atom. This value meets the one estimated with XMCD assuming $\alpha = 0.23 \pm 0.02$ in agreement with previously reported estimates of $\alpha = 0.2$ [117].

Figure 18d shows the particles MAE distribution derived from the perimeter length distribution and the value of E^{ap}. Similar to the size distribution, the K distribution has a Gaussian shape. However, its HWHM is with 17% almost a factor of 2 smaller than the size distribution having 32%. This is explained by the MAE assumed to be given by the perimeter length, which in 2D has a distribution half as wide as the one of the size. The second remarkable feature is that the value of 17% is less than half of the

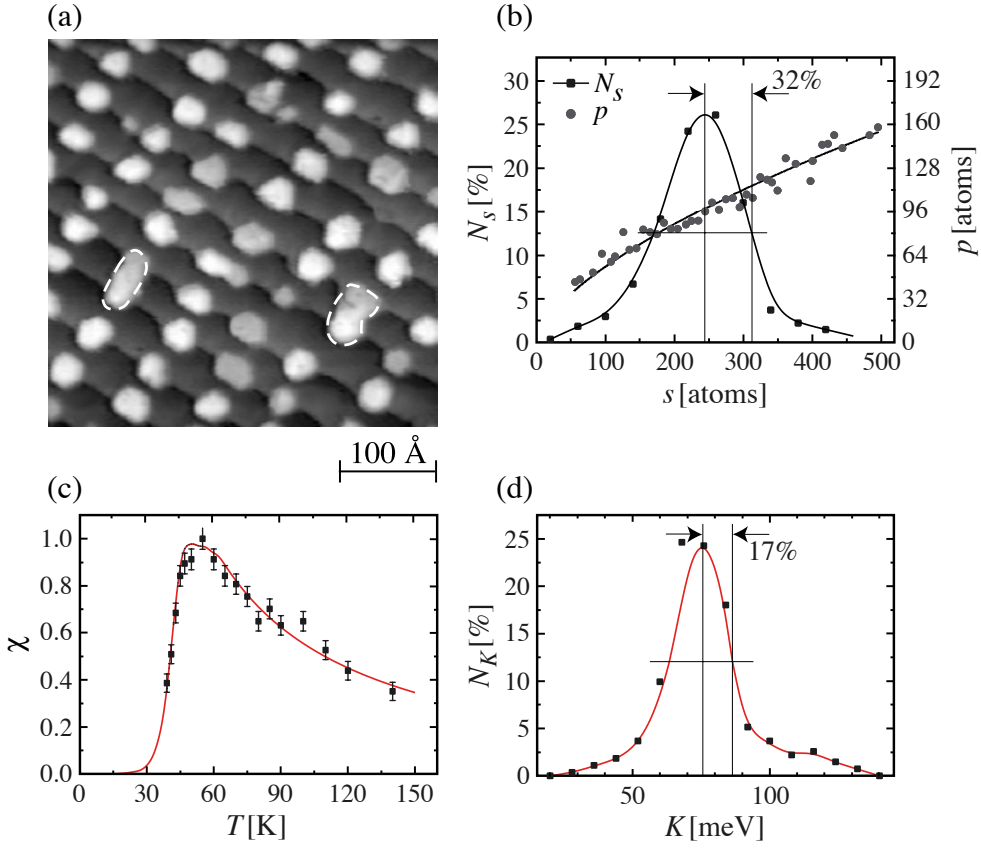

Figure 18: (a) STM image showing the surface morphology for a Co coverage of $\theta = 0.75$ ML. Coalesced islands are encircled by dashed white lines. (b) Size and perimeter length distribution. (c) $\chi(T)$, the solid line represents the fit calculated by assuming K to originate from the perimeter atoms. (d) MAE distribution used to fit $\chi(T)$ in (c) [16].

best result so far achieved for colloid particles [5]. For the 3D colloid particles, the nonuniformity at the surface and the competition between several causes of anisotropy, such as faceting, strain, or shape anisotropy, may give rise to several easy axes per particle. In addition, these axes are randomly oriented from one particle to the next leading to dipolar interactions, which altogether explains the relatively wide anisotropy energy distribution [11]. Figure 18 shows that ordered arrays of uniaxial out-of-plane nanostructures grown by MBE may achieve much more narrow MAE distributions than anticipated based on the size distribution alone [16].

The system is also characterized by negligible dipolar interactions between the islands. Similar to the case of Co/Pt(1 1 1) discussed above, one can exclude interactions in looking at the decay of $\chi(T)$ above T_b. This decay is steeper than $1/T$ as expected for a non-interacting uniaxial system. A second independent evidence for the absence of interactions was derived by growing a sample with a bimodal size distribution due to the coexistence of noncoalesced and coalesced Co islands. For this sample, $\chi(T)$ was reported to display a clear double peak which is only possible if the macrospins of the two island sizes can fluctuate individually [16]. Similar estimations than above of the

stray field of all other islands acting onto a given island suggest that the islands moment can be increased by a factor of 10 still not giving rise to interactions. This is very promising since it theoretically enables an increase of T_b by a factor of 10 and thus realization of a superlattice of uniaxial out-of-plane particles which are blocked up to above room temperature.

4.3. Array of room temperature blocked nanoparticles: Co pillars on Au(1 1 1)

The Co dots on Au(7 8 8) show very good uniformity of the spatial and magnetic properties; however, their blocking temperature of about 50 K is too low to present a model system relevant for applications. A step forward in the direction of producing a long-range ordered array of room temperature blocked nanoparticles was accomplished by Fruchart et al. [41, 119]. The authors succeeded in fabricating vertical self-assembled Co pillars on Au(1 1 1) which increases the size of the Co islands usually grown on Au(1 1 1) and with it their MAE, while keeping the in-plane periodicity unaltered.

The surface morphology following the pillar growth sequence is shown in Fig. 19. As a first step, 0.2 ML Co are deposited on Au(1 1 1) at 300 K which produces 2 ML high Co islands located at the elbows of the herringbone reconstruction. Subsequently, the surface is covered with the amount of Au necessary to fill the space between the islands and to complete 4 ML above the substrate. During this deposition step, the temperature is raised from 425 to 475 K. The distance between bulk hcp Co(0 0 0 1) layers is with 2.05 Å smaller than the one of Au(1 1 1) (2.35 Å). In agreement with this

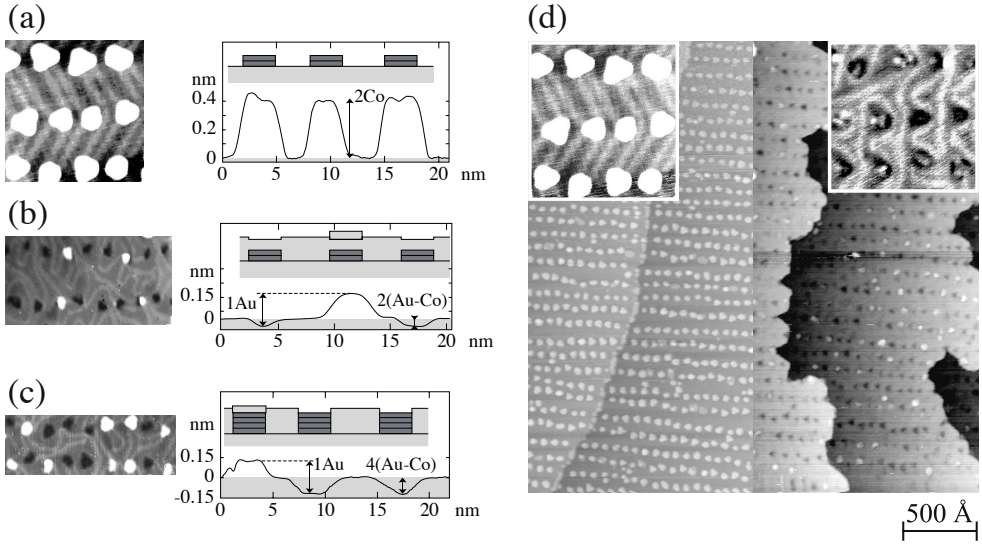

Figure 19: Pillar-growth illustrated by STM views of the uppermost surface layer. For steps (a)–(c) right panels show the surface profile in STM line scans and a schematic sample cross-section. (a) 0.2 ML Co deposited onto Au(1 1 1) at 300 K leads to 2 ML high islands located at the elbows of the Au(1 1 1)–($\sqrt{3} \times 22$) reconstruction (image size 250×250 Å^2). (b) After deposition of Au up to completion of four atomic layers (600×350 Å^2). (c) After deposition of the second layer of Co dots (600×250 Å^2), (d) STM image of ordered 2 ML high Co islands (left) and pillars grown by deposition of 10 Co/Au bilayers (right, different area). Insets show enlargements revealing the Au reconstruction [41, 119].

geometrical consideration, the buried islands appear as an array of 0.6 Å deep hollows (Fig. 19b). As a third step, 0.2 ML of Co are deposited at 500 K. This is the amount of Co needed to increase the height of the previous Co islands by 2 ML. The newly deposited Co atoms displace the Au and go on top of the buried dots, as can be inferred from Fig. 19c. The array now displays hollows and islands. The hollows are about 1.2 Å deep, i.e., four times the difference of layer spacing between Co and Au, suggesting that the dots are now indeed four atomic layers high.

This implies a double-layer place-exchange between deposited Co atoms and Au atoms covering the buried Co dots from the previous layer. Subsequently, the amount of Au required to complete a smooth fifth layer is deposited at 500 K. The situation is then similar to that after step two. Starting from this point and maintaining the temperature at 500 K, the sequence can be repeated and preserves order up to 16 cycles (Fig. 19d). This is consistent with the fabrication of continuous pillars of nearly pure Co on Au(1 1 1) with an aspect ratio of about 2:1 (height over diameter). For 80 Å high pillars, a blocking temperature of 300 K was reported [119]. However, the temperature dependence of the remanent magnetization suggested magnetic interactions between adjacent pillars, which could contribute to the observed high blocking temperature.

5. MAE AND MAGNETIC MOMENT OF SINGLE ATOMS

In the previous sections, we discussed examples demonstrating the link between magnetic properties and atomic coordination. Moving from bulk ferromagnets to the edge atoms of 2D islands deposited on low-index single-crystal metal surfaces may increase the MAE from a few tens of μeV/atom to 1 meV/atom. This trend is expected to continue moving from small islands, where the lateral coordination is still 2–6 down to single adatoms. Recent experiments [46] confirmed calculations predicting magnetic anisotropies of the order of 10 meV/atom [120, 121], i.e., 10^3 times larger than bulk anisotropies.

Adatoms due to their zero lateral coordination are predicted to have spin and orbital magnetic moments in-between those of bulk compounds and free atoms [120, 122]. Gas-phase transition metal (TM) atoms possess large m_S and m_L, according to Hunds rules, which are due to intra-atomic Coulomb interactions. In a solid, electron delocalization and crystal field effects compete with these interactions, causing a substantial decrease of m_S and partial or total quenching of m_L. Such effects have been predicted to be strongly reduced in TM impurities at non-magnetic surfaces owing to the decreased coordination [120], with implications also for the appearance of significant magnetic anisotropy. TM clusters in the gas phase have shown a strong dependence of the total magnetic moment ($m_S + m_L$) on the particle size [123, 124].

In the first part of this section, we discuss the XMCD results of Co adatoms and small islands on Pt(1 1 1), giving hard experimental numbers on K, m_L, and m_S, for single adatoms up to islands of 40 atoms. We then turn to Fe, Co, and Ni adatoms on K thin films showing different degrees of hybridization revealing the electronic ground state configuration.

5.1. Single Co atoms and small islands on Pt(1 1 1)

Single atoms and small islands have been created by statistical and kinetically controlled growth of Co on Pt(1 1 1) [37]. The Co/Pt system was chosen in order to

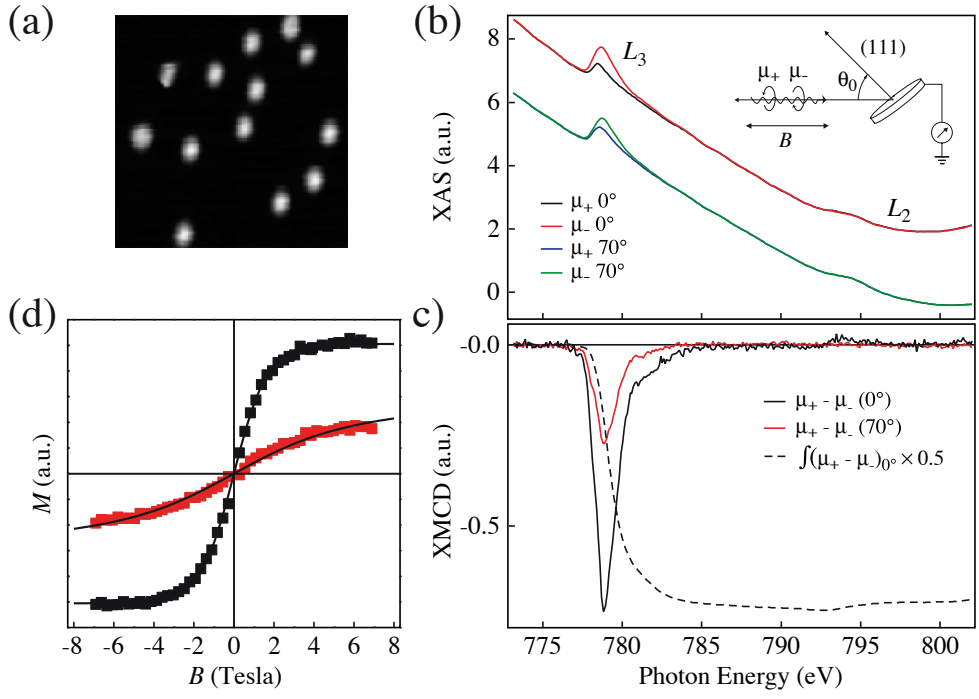

Figure 20: (a) STM image of isolated Co adatoms on Pt(1 1 1) ($\theta = 0.010$ ML, 85×85 Å). (b) $L_{3,2}$ XAS spectra of sample shown in (a) ($T = 5.5 \pm 0.5$ K, $B = 7$ T). (c) Magnetization curves at $\theta_0 = 0°$ (black symbols) and $\theta_0 = 70°$ (gray symbols) ($T = 5.5$ K). (d) XMCD spectra ($\mu_+ - \mu_-$) obtained for $\theta_0 = 0$ and 70°. The dashed line is the integrated XMCD at $\theta_0 = 0°$ [46].

maximize the MAE effects, since hcp-Co presents the largest MAE among 3d ferromagnetic elements (0.045 meV/atom compared with, e.g., 0.005 meV/atom for Fe). In addition, CoPt alloying in the bulk-ordered $L1_0$ phase results in an MAE increase up to 0.8 meV/Co atom [125], owing to the strong spin–orbit coupling of the Pt 5d states. Figure 20a shows an STM image of isolated Co adatoms obtained by depositing 0.01 ML at $T = 5.5$ K, for which thermal surface diffusion is completely inhibited. Figure 20b shows the XAS spectra of the Co $L_{2,3}$ edges using left and right circularly polarized light in the total electron yield mode. The XMCD signal (Fig. 20d) is the difference between the XAS spectra recorded for parallel (μ_+) and anti-parallel (μ_-) alignment of the photon helicity with respect to the applied field B. Fields of up to 7 T were used to magnetize the sample. For $\theta_0 = 0°$ field and light are along the surface normal, for 70° the sample is strongly tilted as shown in the inset of Fig. 20b. The spectra at $\theta_0 = 70°$ have been normalized to the $(\mu_+ + \mu_-)$–L_3 intensity at $\theta_0 = 0°$ in order to eliminate the dependence of the electron yield on the sample orientation.

The XAS spectra show relatively weak absorption features compared with the Pt background due to the extremely low concentration of Co adatoms. However, the XMCD signal is very large relative to the total Co absorption signal, indicating the presence of strong magnetic moments localized at the Co atoms. Two magnetic properties are characteristic of the single Co adatoms. First, the vanishing intensity of the XMCD at the L_2 edge indicates unusually strong orbital magnetism. Second, the large

difference between the in-plane and out-of-plane $M(B)$ curves (Fig. 20c) reveals an extraordinary MAE. According to the XMCD sum rules [111, 112, 115], $m_L = 1.1 \pm 0.1\ \mu_B$/atom is measured along to the easy axis ($\theta_0 = 0°$) [46]. This value is smaller than $3\ \mu_B$ of a gas-phase Co atom, but much higher than in bulk, where m_L is usually reduced to 0.1–0.2 μ_B owing to the hybridization of the d-states. The explanation lies with the reduced coordination of an isolated atom adsorbed on top of a flat surface, favoring d-electron localization and thus the survival of atomic-like character in the 3d orbitals. The presence of such a large orbital magnetization has significant consequences for the magnetic anisotropy.

The MAE E_a was determined by measuring the component of the adatom magnetization parallel to B, with B applied along the surface normal and tilted to it by $\theta_0 = 70°$. The data points in Fig. 20c represent the peak of the L_3 XMCD intensity at 778.6 eV divided by the pre-edge intensity at 775 eV as a function of B, which corresponds to a good approximation to $M(B)$. The difference between the $\theta_0 = 0°$ and $\theta_0 = 70°$ curves is consistent with the XAS-normalized XMCD spectra. The solid lines are Langevin fits to the data assuming uniaxial anisotropy yielding $E_a = 9.3 \pm 1.6$ meV/atom, which is an exceptionally large value [46]. Typical systems with high MAE are $SmCo_5$ ($E_a = 1.8$ meV/Co atom [125]), Co/Pt, Co/Au multilayers ($E_a \approx 0.3$ meV/Co atom [44, 117]), and 1D Co atomic chains ($E_a = 2.0$ meV/Co atom [59]). Different effects combine in establishing the magnitude of the MAE for the Co adatoms. The reduced coordination leads to 3d-electron localization (band narrowing), which augments the spin–orbit energy due to increases in the local density of states near the Fermi level and the orbital and spin magnetic moment [116, 126].

The influence of the atomic coordination on the MAE and m_L is revealed by measurements on small 2D islands. Figure 21 reports m_L and E_a as a function of n for Co_n/Pt(1 1 1). The smaller n, the larger are the m_L and E_a dependences on changes of the cluster size. Particles with $n = 3$ and 4 atoms have m_L reduced to 0.78 ± 0.05 and $0.59 \pm 0.05\ \mu_B$/atom, respectively. One-atom variations of the particle size cause significant reductions of E_a: for $n = 3$ atoms, $E_a = 3.3 \pm 0.4$ meV/atom, only about 30%

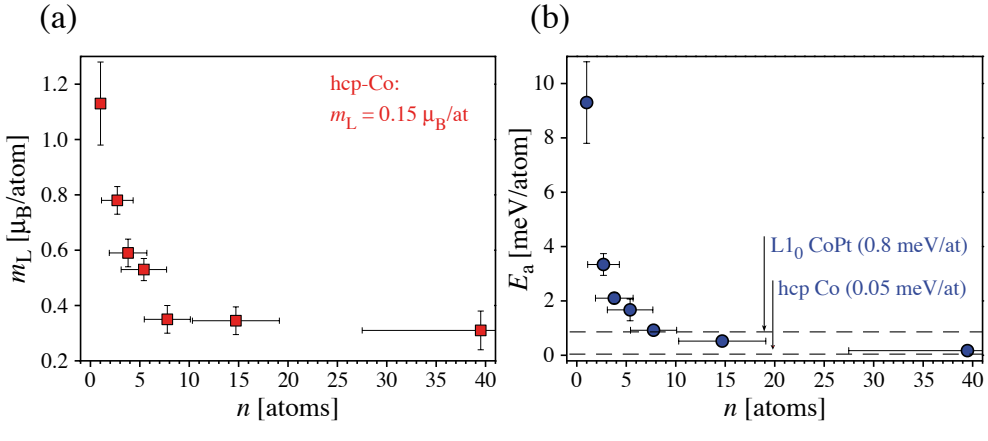

Figure 21: (a) m_L and (b) E_a as a function of average island size n for Co_n/Pt(1 1 1). For comparison, the dashed lines show E_a of the L_{10} CoPt alloy and hcp-Co, respectively. The error bars on the horizontal scale represent the standard deviation of the size distribution as determined by STM [46].

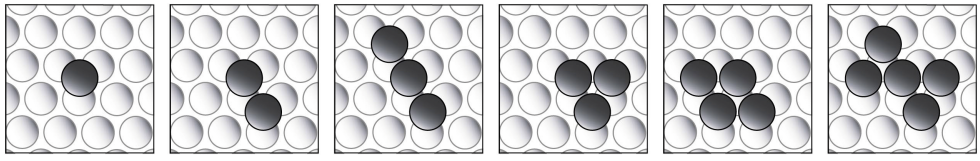

+18 meV	+4.1 meV	+3.7 meV	+2.2 meV	+0.75 meV	+1.8 meV
0.60 (1.05) μ_B	0.38 (0.74) μ_B	0.34 (0.67) μ_B	0.25 μ_B	0.22 μ_B	0.27 μ_B

Figure 22: Ab initio calculations of E_a and m_L for Co/Pt(1 1 1) using the spin-polarized-relativistic Korringa–Kohn–Rostocker Greens function method in the spin-density approximation [46]. The Co atoms are on fcc sites. The m_L values in brackets have been computed within the orbital polarization scheme with a 50% reduced Racah parameter. The reported values are averages over all constituent atoms, atoms at different sites within the islands may well have relevant differences in E_a and m_L (see Ref. [127]).

of the single adatom value. Ab initio calculations show that the atomic coordination rather than the absolute particle size is the key to determine m_L and E_a [46, 127] (see Fig. 22). In the experiment, different shapes coexist for each cluster size and the size distribution has a finite width. This makes impossible discerning anisotropies of, e.g., elongated from triangular trimers, having according to the calculations 3.7 and 2.2 meV/atom, respectively.

Comparison between Fig. 21a and b also demonstrates the correlation between m_L and E_a, as expected from a perturbative treatment of the spin–orbit interaction. According to Bruno [116] and van der Laan [126] E_a is directly related to the anisotropy of m_L, and in TM atoms with more than half-filled d-shells the easy axis is the direction where m_L is maximum. In the experiment, the incomplete saturation of the magnetization close to the direction of the hard axis (Fig. 20c) does not allow a precise estimate of the m_L anisotropy via the XMCD sum rule for the orbital moment. However, it is clear that a large m_L anisotropy, hence large E_a values, can be observed only if m_L itself is large, thus explaining the observed correlation between E_a and m_L reported in Fig. 21. In addition to the large orbital moment of Co, the magnetization induced in the substrate creates additional MAE due to the strong spin–orbit coupling of the Pt 5d-states, an effect common to CoPt compounds [128]. The effect of the interaction with the substrate is well revealed by the quite different magnetic properties observed for Co adatoms on alkali metal films, for example K. In contrast to Pt, the outer electronic shell of K has *s*-character, i.e. $L = 0$. In this case the spin–orbit interaction is expected to be absent.

5.2. Magnetic impurities on alkali metals

The degree of hybridization of the electronic states of magnetic adatoms or of very small islands with the substrate determines to which extent the magnetic properties are described by discrete values of the magnetization or by a continuum of values, as in classical magnets. The magnetization as a function of external field under equilibrium conditions is in the first case described by the Brillouin function in the latter by the Langevin function. The fact that the Langevin function had to be used for Co/Pt(1 1 1) suggests that the Co moments behave as classical magnetization vectors emerged in an anisotropy potential energy surface created by the substrate lattice. It is anticipated that under these conditions magnetization reversal takes place by crossing of the

anisotropy barrier, and not by tunneling, as e.g. observed for single molecule magnets which couple less strongly to their environment [129]. Similarly, single adatoms on metal surfaces covered by a few monolayer thick oxide films are expected to have less hybridization, to preserve more of their atomic electronic structure and consequently to show stronger effects of quantization of the magnetic moment [130].

The differences of hybridization and electronic ground state configuration become apparent when comparing different magnetic adatoms on different metal hosts. We discuss XAS and XMCD data probing the local electronic and magnetic structure of Fe, Co, and Ni impurities deposited on K and Na films [131]. K and Na films were evaporated onto a clean Cu(1 1 1) substrate. Transition metals were subsequently deposited in minute quantities, 0.002–0.015 ML, at $T = 10\,\mathrm{K}$ in order to obtain isolated impurities. XAS at the $L_{2,3}$ edges was performed in total electron yield mode using circularly polarized light with 99% polarization in magnetic fields up to $B = \pm 7\,\mathrm{T}$ with the sample at $T = 10\,\mathrm{K}$.

Figure 23 shows the XAS and XMCD spectra recorded for Fe, Co, and Ni impurities deposited on a K film. The XAS spectra present narrow multiplet structures which are not observed for single Co atoms on Pt(1 1 1). This is a clear indication of a strong localization of the 3d electrons on the transition metal impurities. The multiplet structure serves as a sensitive fingerprint of the electronic ground state configuration which can be determined by comparison of the experimental spectra with those calculated by atomic multiplet theory. The spectra shown as insets correspond to the $3d^n \rightarrow 2p^5 3d^{n+1}$ transitions calculated in zero crystal field with an atomic value for the spin–orbit splitting. The comparison of experiment and theory allows unambiguous determination of the respective ground states, i.e., d^7 ($^4F_{9/2}$) for Fe, d^8 ($^3F_4$) for Co, and d^9 ($^2D_{5/2}$) for Ni. These correspond to a magnetic moment $m = g_J \mu_B \sqrt{J(J+1)}$ (here J denotes the generalized angular momentum and not the magnetic exchange

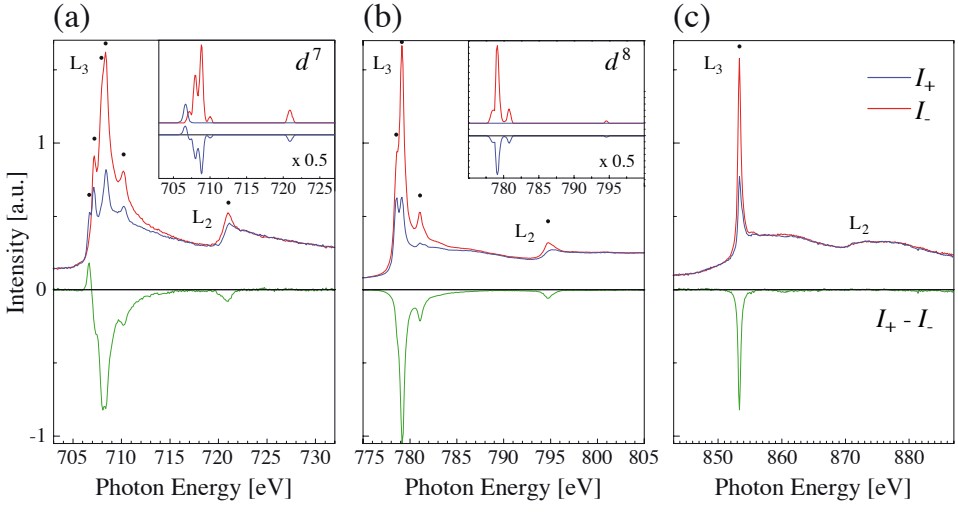

Figure 23: XAS and XMCD spectra of the $L_{2,3}$ edges recorded with parallel (solid line) and anti-parallel (dashed line) alignment of the light helicity with respect to the field direction. (a) 0.015 ML Fe, (b) 0.015 ML Co, and (c) 0.004 ML Ni deposited on K films. The insets of (a) and (b) show the corresponding calculated spectra [132] for atomic d^7 and d^8 configurations [131].

energy as above) of about 6.6 μ_B for Fe, 5.6 μ_B for Co, and 3.6 μ_B for Ni. These values are sensibly higher than the bulk values of 2.2 μ_B, 1.7 μ_B, and 0.6 μ_B, respectively. Another interesting feature is represented by the XMCD at the L_2 edge which has opposite sign with respect to bulk spectra for Fe and Co, whereas it is zero for Ni. The last observation is understood from the ground state configuration d^9 which does not allow L_2 edge transitions, corresponding to the $J = 5/2 \rightarrow J = 1/2$ excitation which is forbidden by the dipole selection rule [133].

6. SPATIALLY RESOLVED MEASUREMENTS OF SPIN POLARIZATION OF MAGNETIC ISLANDS

Magnetic random access memories (MRAMs) will possibly replace our current dynamic random access memories (DRAM) due to their shorter access time, and to the fact that they are non-volatile [134]. A typical MRAM architecture consists of an array of magnetic cells, each consisting of two ferromagnetic layers separated by an insulating barrier. The cells can be designed so that the magnetic moments of the two layers can be parallel or anti-parallel. These states allow a bit of information to be stored. The magnetization of one electrode of the spin-valve is pinned by exchange bias [135], while the orientation of the magnetization of the free layer is controlled by magnetic fields generated by electrical currents. The state of the cells is read by the tunnel magnetoresistance (TMR). In recent literature, the TMR is defined as $(R_a - R_p)/R_p$, with R_a and R_p being the junction resistance for anti-parallel and parallel magnetization of the two ferromagnets, respectively.

MRAMs began to be considered seriously when two groups reported TMR values of 10% at room temperature [136, 137]. The breakthrough was achieved by using amorphous aluminum oxide barriers to make pin-hole-free tunnel barriers. Calculations suggested that much higher values of TMR could be realized by using crystalline rather than amorphous barriers [138, 139]. It was predicted that tunneling through crystalline barriers of materials depends strongly on the symmetry of the wave functions at the Fermi energy. It turns out that the states with the most symmetric wave functions can get through certain barriers much more easily than states with lower symmetry. Some ferromagnetic materials, for example, body-centered-cubic (bcc) Fe, FeCo, and Co, have the property that the high-symmetry state is present for the electrons with majority spin but not for minority electrons. When the moments are parallel, the high-symmetry majority electrons can get through the barrier and enter the electrode on the other side. When the moments are anti-parallel, the high-symmetry majority electrons in one electrode can get through the barrier, but they cannot enter the electrode on the other side unless there is a scattering event that breaks the symmetry. Experimentally, very large values of TMR at room temperature have recently been reported. By using molecular beam epitaxy to produce crystalline interfaces, TMRs of 220 and 410% have been observed with Fe(1 0 0)/MgO(1 0 0)/Fe(1 0 0) [140] and Co(1 0 0)/MgO(1 0 0)/Co(1 0 0) [141] magnetic tunneling junctions.

Nanoparticles could play a leading role in the development of future MRAMs. When magnetic nanoclusters are deposited on a non-magnetic substrate charge transfer, multiple electronic scattering and interference phenomena generally govern the electronic and the magnetic properties of the combined system. For example, surface states of non-magnetic noble metal substrates, such as Cu(1 1 1), turn spin polarized

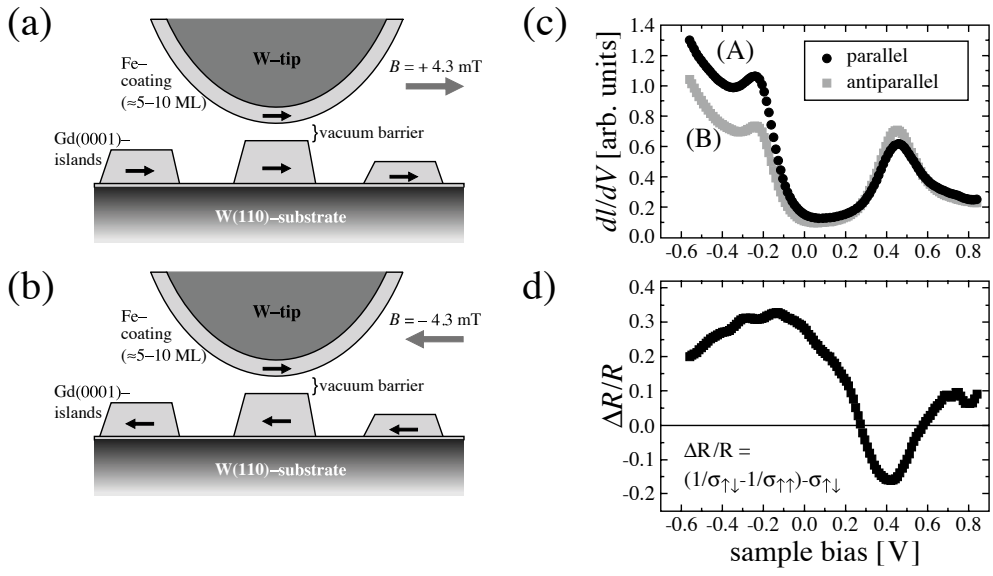

Figure 24: (a) and (b) Schematic drawing of the experimental setup for measuring the vacuum TMR between an Fe-coated W tip and a Gd(0 0 0 1) island on W(1 1 0). (c) Tunnel conductance dI/dV for parallel and anti-parallel alignment of tip and sample magnetization ($T = 70$ K). (d) Resistance changes as function of bias voltage [142].

and attain a different character when Co nanoislands are added to the substrate surface [94, 95]. Such spin-polarized surface states (SP-SS) can serve as spin-transport channels across the vacuum barrier to or from another magnetic material, an issue which is of central importance for spintronic applications based on spin-polarized tunneling. STM experiments by Wiesendanger et al. indicate that TMR is maximized by tunneling to a SP-SS [142]. The experimental situation is schematically depicted in Fig. 24. An Fe-coated W tip, prepared by in situ thin-film deposition in a UHV system containing a variable-temperature STM, is positioned above a Gd(0 0 0 1) island grown on a W(1 1 0) substrate. Gd islands of a few 100 nm diameter exhibit a very low coercivity on the order of 11 mT. Therefore, an external field of a few mT applied in the sample plane was found to be sufficient for switching the magnetization direction of the Gd islands while leaving the magnetization state of the Fe coated tip unaffected. With the feedback loop open, the bias voltage V was ramped between –0.6 and 0.8 V and the differential conductance dI/dV(V) was measured. This signal is approximately proportional to the LDOS at the position of the tip.

Figure 24c shows two conductance curves corresponding to the experimental situations depicted in Fig. 24a and b. Pronounced maxima are observed in both spectra at $V_1 = -0.2$ V and $V_2 = 0.45$ V corresponding to the energies of the two spin components of an exchange-split d_{z^2} surface state of Gd(0 0 0 1). The asymmetry between spectrum (A) and (B) is due to the spin-valve effect enhancing the conductance for the surface-state spin component being parallel to the majority spin states of the tip and

reducing it for the anti-parallel component. The resistance change as function of bias voltage is plotted in Fig. 24d. It reaches 31% (TMR = 45%) for the filled and 13% for the empty part of the two spin components of the exchange-split surface state.

TMR values up to 850% were reported for STM tunnel junctions formed by out-of-plane magnetized ferromagnetic bilayer Co islands on Pt(1 1 1) and an anti-ferromagnetic Cr-coated W-tip [143]. Co double-layer islands were created by deposition of 0.40 ML on the Pt(1 1 1) substrate held at 130 K and subsequent annealing to 340 K [39]. The –9.4% misfit between Co and Pt leads to partial dislocations in the first layer [58], whereas in double-layer islands the stress is relieved by a moiré structure [144, 145], see the superstructure on-top of the islands in Fig. 25a. When imaged with a Cr-coated W-tip, in addition to the corrugation of the moiré, one clearly discerns two island species by an apparent height difference (see Fig. 25b). This contrast is magnetic since it is only obtained with magnetic tips (either Cr-coated W-tips, or NiMn bulk-tips), and it vanishes above the island blocking temperature of $T_b = 180$ K, independently determined by means of MOKE measurements [39]. The MOKE measurements also reveal out-of-plane magnetization in agreement with the fact that spin

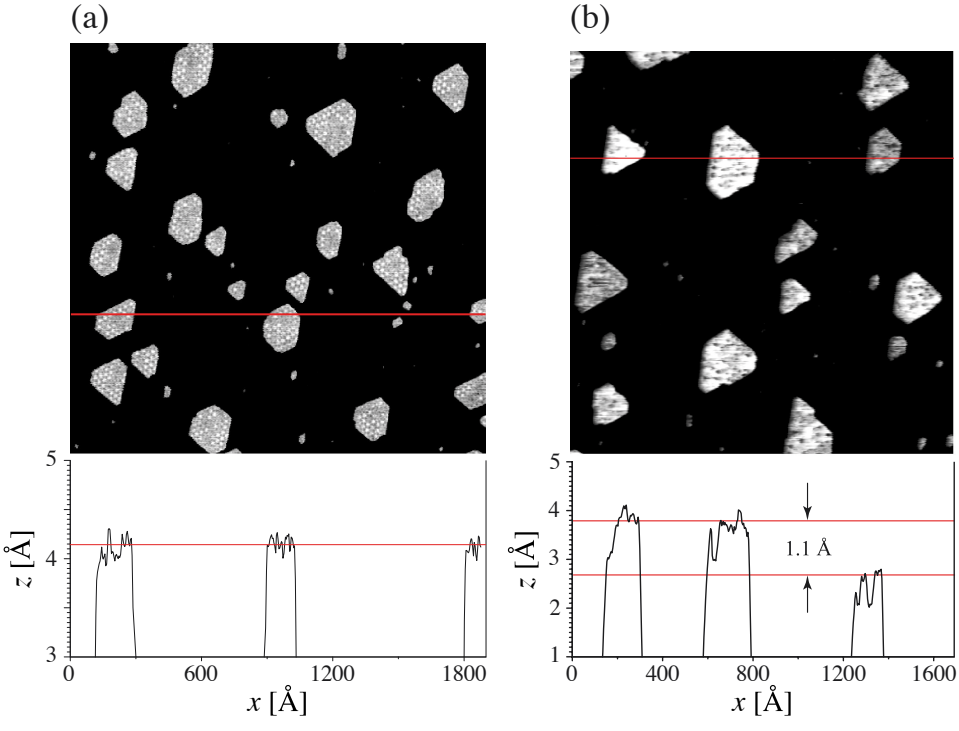

Figure 25: (a) Constant current STM image of double-layer Co islands recorded with a bare W tip. The moiré structure has an apparent height corrugation of 0.30 ± 0.03 Å ($T_{sample} = 140$ K, $V_t = -0.2$ V and $I_t = 1.0$ nA). (Bottom panel) Constant current profile obtained by averaging over ±5 line scans around the marked position. All islands appear with identical heights irrespective of their magnetization (absence of spin contrast). (b) Constant current STM image of double-layer Co islands recorded with a Cr-coated W tip ($T_{sample} = 140$ K, $T_{tip} \approx 280$ K, $V_t = -0.2$ V, $I_t = 0.3$ nA). (Bottom) Averaged (±5 lines) line scan at the indicated position revealing a surprisingly high difference of 1.1 ± 0.1 Å in the apparent height of islands with opposite magnetization [143, 147].

contrast is only observed with a Cr coating thickness of 20–40 ML reported to give out-of-plane polarization of the tip [146]. The magnetic contrast typically amounts to $\Delta z = 0.20 \pm 0.05$ Å, but occasionally values as high as $\Delta z = 1.1 \pm 0.1$ Å were also measured (see Fig. 25b). The contrast in apparent height can be converted into a TMR-value as follows:

$$\Delta R/R = \frac{R_a - R_p}{R_p} = \frac{I_p}{I_a} - 1 = \exp(A\sqrt{\phi}\Delta z) - 1 \tag{6}$$

where ϕ is the average over the work-functions of tip and sample and $A = 2\sqrt{2m_e/h^2} = 1.025\ \mathrm{eV}^{-1/2}\ \mathrm{Å}^{-1}$. Assuming a typical value of $\phi = 4$ eV yields TMR values of $\Delta R/R = 50 \pm 15\%$ for $\Delta z = 0.2$ Å and $\Delta R/R = 850 \pm 200\%$ for $\Delta z = 1.1$ Å, respectively.

The junction polarization is derived from the magnetic contrast by

$$P = P_t P_S = \frac{I_p - I_a}{I_p + I_a} = \frac{\exp(A\sqrt{\phi}\Delta z) - 1}{\exp(A\sqrt{\phi}\Delta z) + 1} \tag{7}$$

One finds $P = 0.20 \pm 0.05$ and 0.80 ± 0.04 for $\Delta z = 0.20 \pm 0.05$ Å and $\Delta z = 1.1 \pm 0.1$ Å, respectively. $P = 0.20 \pm 0.05$ is comparable with polarization values reported between Co(0 0 0 1) surfaces and amorphous Co-based alloy tips [148]. However, 80% polarization of the tunnel barrier implies a polarization of the Co islands of at least 80%, about two times larger than the value determined by Andreev reflection for Co bulk [149, 150]. This can be rationalized by the low dimensionality of the islands increasing the density of states at the Fermi level, or by k-selective tunneling leading to a higher polarization than the state averaged value. The strong polarization of the tip, which must have been close to 100% in this experiment, can possibly be caused by chemisorbed species at the tip apex.

Recently, a theoretical work suggested the modulation and control of the spin-polarized surface states based on an appropriate design of the nanostructure geometry, such as the size of the islands [151]. The idea consists in the spatial and energetic tuning of the spin polarization of islands by means of quantum confinement. Figure 26 reports the result of calculations for equilateral triangular islands of Co on Cu(1 1 1).

This prediction was experimentally confirmed by Pietzsch et al. by using a low-temperature STM with a Cr-coated W-tip [152]. Figures 27a and b show dI/dV maps at bias voltages allowing to observe the standing wave patterns on both the Cu substrate and on the Co islands. The contrasts between islands are due to their magnetization being oriented either up or down, that is, parallel or anti-parallel to the tip magnetization. The contrast inversion between (a) and (b) is not caused by a magnetization reversal of either tip or sample, but is the result of contributions to the LDOS from states of opposite spin, their relative weights depending on the applied bias. The chromium at the tip has an electronic structure dominated by minority spin states near the Fermi level [153], allowing a very effective tunneling between tip and sample minority states for parallel magnetization of both electrodes. The bias voltage of Fig. 27a has been chosen in a range where the main contribution to the sample LDOS comes from the dispersive majority spin state which is responsible for the

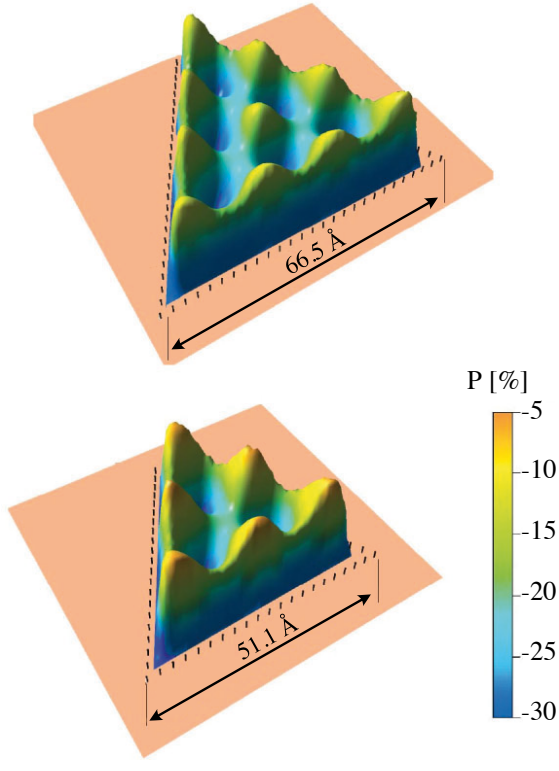

Figure 26: Spin polarization of surface-state electrons on triangular Co islands on Cu(1 1 1); calculations are performed for $E = 0.5\,\text{eV}$ above E_F [151].

standing wave pattern. Therefore, the islands exhibit inverted contrast for energies higher than about –0.065 eV.

In a narrow energy window between 0.18 and 0.43 eV above the Fermi level, the islands return to normal spin contrast as shown in Fig. 27b. In this interval an unoccupied localized minority spin d-state outweighs the majority band. Figure 27c also shows the effect of electron confinement, manifest in the evolution of the standing wave periods as a function of bias voltage. The inset of Fig. 27c allows for a comparison of the dispersive behavior of the Co islands and the Cu substrate. Both data sets were fitted (solid lines) assuming a 2D free electron gas, confined for Co but not for Cu. While the Cu values match the fit parabola very well, the Co data display a steplike structure. The effect of SP-SS on the Co patterns is displayed in Fig. 27d showing $\mathrm{d}I/\mathrm{d}V$ profiles taken along lines as indicated in Fig. 27a for bias voltages being representative for ranges of inverse, balanced, and normal spin contrast. In each case, the standing wave amplitude is found to be significantly larger on the anti-parallel island, regardless of the sign of the bias-dependent spin-polarization. The amplitude ratios of the parallel and anti-parallel case are 0.49, 0.40, and 0.32 at the respective voltages. Qualitatively, this behavior is explained as follows. Because the tip has an effective negative SP within the energy range relevant for the standing wave observation, tunneling into the oscillatory majority surface state band is not very efficient for the parallel configuration. By contrast, in anti-parallel magnetized islands,

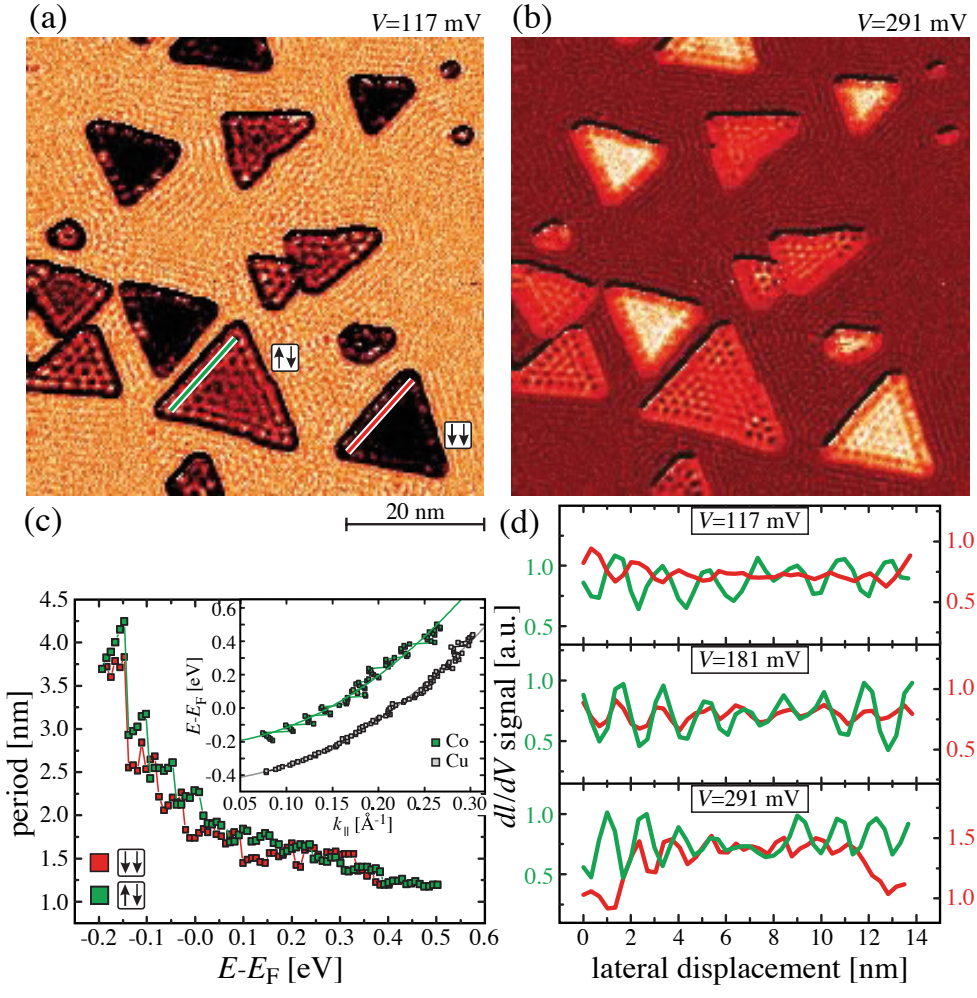

Figure 27: Co islands on Cu(111) ($\theta = 0.6$ ML, $T = 14$ K). (a) and (b) dI/dV maps at indicated bias voltages showing standing wave patterns on Cu substrate and Co islands. Arrows indicate parallel ($\uparrow\uparrow$) or anti-parallel ($\uparrow\downarrow$) magnetization of islands and tip. (c) Standing wave periods on Co islands as a function of bias voltage. (Inset) E–E_F vs. $k_{\|}$ for Co and Cu. (d) dI/dV profiles taken along lines indicated in (a). Regardless of the bias voltage, the standing wave amplitude is larger on the anti-parallel island [152].

the role of minority and majority spins is exchanged with respect to the tip. As a consequence, the oscillatory state in anti-parallel islands has the matching spin character for an effective tunneling of the excess tip minority spin electrons, resulting in an enhanced scattering amplitude. Only delocalized sample majority electrons take part in the LDOS oscillations while localized minority d-like electrons do not. Still, the net balance of contributions from majority and minority states to the sample LDOS determines the overall contrast between the islands which may be normal or inverted (or balanced at the point of sign inversion), depending on the bias voltage; the standing wave pattern is then superimposed onto this background signal.

The experimental data did not reveal any spin-induced modification of the Cu oscillation pattern in the immediate vicinity of oppositely magnetized Co islands.

However, a remarkable feature was found in the island rims. The spin character of the rim state is opposite to that exhibited by the island at the corresponding energy, emphasizing that the spin polarization, on a lateral scale of a few angstroms, may not only change its magnitude but also its sign, depending on the electronic states involved.

7. CONCLUSIONS AND OUTLOOK

Experiments of small well-defined magnetic islands have significantly improved our understanding of orbital magnetism. Orbital moments and anisotropy energies have been determined for Co/Pt(1 1 1) as function of island size from single atoms up to large islands. They reveal a direct link between preserved orbital moments in low-coordinated atoms and their high anisotropy. From thin film studies these effects were anticipated, however, the order of magnitude of the anisotropies was a surprise. Co step atoms reach anisotropies of very hard magnetic alloys and Co adatoms have 10 times higher values. This implies blocking temperatures of Co monomers of $T_b = 4.3\,\mathrm{K}$ ($K = 9.3\,\mathrm{meV}$), while due to the steep decrease of anisotropy with increasing coordination a Co heptamer has $T_b = 3.2\,\mathrm{K}$ ($K = 7\,\mathrm{meV}$). By contrast, due to the different moments, the coercitive field of monomers ($m = 5\,\mu_B$) is 32 T, while the one of heptamer ($m = 21\,\mu_B$) is 6 T.

For larger islands, the mechanism of thermal magnetization reversal has been seen to vary from system to system. As anticipated, compact islands show coherent rotation up to larger sizes than ramified ones. Also, the Curie temperatures of the first are larger than for the latter. The transition between the two reversal modes can be calculated knowing the exchange stiffness J, which is only known for bulk and films of several ML thickness. Therefore, SP-STM measurements of the width of domain walls in monolayer films are very valuable.

SP-STM has been developed as a reliable tool for the determination of spin-polarization and tunnel magneto-resistance of junctions with 2D islands. However, de-convolution of tip and sample polarizations remains a challenge and one has to rely on calculations. SP-STM may also be used in the future to locally check whether the above-mentioned blocking temperatures are indeed characterizing individual islands. This is worthwhile since thermal magnetization reversal may take place along a direction of M which has not been explored in the XMCD measurements of K. Whether single magnetic atoms or small islands behave a classical moment or have quantized orientations of M, and under which conditions they reverse by thermally activated barrier crossing or by tunneling depends on the interaction with the substrate and is expected to vary from metals to insulators.

Although progress has been made, the self-assembly of regular lattices of uniaxial out-of-plane islands with $T_b = 350\,\mathrm{K}$, absence of dipolar interactions, and narrow distributions of K and M continues to be a challenge. New promising template surfaces have been discovered possibly enabling also the growth of superlattices of bi-metallic particles. Bi-metallic islands promise to have higher anisotropies for given size and therefore will be interesting to investigate again by combination of atomic scale and spatially integrating techniques. At the end, one would like to grow upstanding pillars since then also the shape anisotropy favors out-of-plane easy axis and the pillars can reach high blocking temperatures while taking only little space in the sample plane.

REFERENCES

[1] Chou S.Y., IEEE Proc. 85 (1997) 652.
[2] Harris J., Awschalom D., Phys. World 12 (1999) 19.
[3] Albrecht M., Rettner C., Moser A., Best M., Terris B., Appl. Phys. Lett. 81 (2002) 2875.
[4] Plumer M.L., van Ek J., Weller D. (eds), The Physics of Ultra-High-Density Magnetic Recording, Springer Series in Surface Sciences, Vol. 41, Springer, Berlin, 2001.
[5] Woods S.I., Kirtley J.R., Sun S., Koch R.H., Phys. Rev. Lett. 87 (2001) 137205.
[6] Petit C., Taleb A., Pileni M., Adv. Mater. 10 (1998) 259.
[7] Puntes V., Krishnan J., Appl. Phys. Lett. 78 (1999) 2187.
[8] Petit C., Rusponi S., Brune H., J. Appl. Phys. 95 (2004) 4251.
[9] Antoniak C., Lindner J., Spasova M., Sudfeld D., Acet M., Farle M., Fauth K., Wiedwald U., Boyen H.G., Ziemann P., Wilhelm F., Rogalev A., Sun S. Phys. Rev. Lett 97 (2006) 117201.
[10] Jamet M., Wernsdorfer W., Thirion C., Mailly D., Dupuis V., Mélinon P., Pérez A., Phys. Rev. Lett. 86 (2001) 4676.
[11] Held G.A., Grinstein G., Doyle H., Sun S., Murray C.B., Phys. Rev. B 64 (2001) 012408.
[12] Sun S., Murray C., Weller D., Folks L., Moser A., Science 287 (2000) 1989.
[13] Black C.T., Murray C.B., Sandstrom R.L., Sun S., Science 290 (2000) 1131.
[14] Brune H., Giovannini M., Bromann K., Kern K., Nature 394 (1998) 451.
[15] Repain V., Baudot G., Ellmer H., Rousset S., Europhys. Lett. 58 (2002) 730.
[16] Weiss N., Cren T., Epple M., Rusponi S., Baudot G., Rohart S., Tejeda A., Repain V., Rousset S., Ohresser P., Scheurer F., Bencok P., Brune H., Phys. Rev. Lett. 95 (2005) 157204.
[17] Bansmann J., Baker S.H., Binns C., Blackman J.A., Bucher J.P., Dorantes-Dávila J., Dupuis V., Favre L., Kechrakos D., Kleibert A., Meiwes-Broer K.H., Pastor G.M., Perez A., Toulemonde O., Trohidou K.N., Tuaillon J., Xie Y., Surf. Sci. Rep. 56 (2005) 189.
[18] Himpsel F.J., Ortega J.E., Mankey G.J., Willis R.F., Adv. Phys. 47 (1998) 511.
[19] Hopster H., Oepen H.P. (eds), Magnetic Microscopy of Nanostructures, Nanoscience and Technology, Springer, Berlin, 2005.
[20] Sellmyer D.J., Skomski R. (eds), Advanced Magnetic Nanostructures, Springer, 2006.
[21] Bell G.M., Lavis D.A., Statistical Mechanics of Lattice Models, Vol. 1, Ellis Horwood Limited, Chichester, 1989.
[22] Wernsdorfer W., Orozco E.B., Hasselbach K., Benoit A., Barbara B., Demoncy N., Loiseau A., Pascard H., Mailly D., Phys. Rev. Lett. 78 (1997) 1791.
[23] Neel I., Ann. Geophys. 5 (1949) 99.
[24] Brown W., Phys. Rev. 130 (1963) 1677.
[25] Bode M., Pietzsch O., Kubetzka A., Wiesendanger R., Phys. Rev. Lett. 92 (2004) 067201.
[26] Braun H.-B., Phys. Rev. Lett. 71 (1993) 3557.
[27] Braun H.-B., Phys. Rev. B 50 (1994) 16485.
[28] Braun H.-B., Phys. Rev. B 50 (1994) 16501.
[29] Braun H.-B., J. Appl. Phys. 85 (1999) 6172.
[30] Brown G., Novotny M.A., Rikvold P.A., Phys. Rev. B 64 (2001) 134422.
[31] Forster H., Bertram N., Wang X., Dittrich R., Schrefl T., J. Magn. Magn. Mater. 267 (2003) 69.
[32] Khapikov A.F., J. Appl. Phys. 89 (2001) 7454.
[33] Cowburn R., Koltsov D., Adeyeye A., Welland M., Phys. Rev. Lett. 83 (1999) 1042.
[34] Yamasaki A., Wulfhekel W., Hertel R., Suga S., Kirschner J., Phys. Rev. Lett. 91 (2003) 127201.
[35] Aharoni A., Introduction to the Theory of Ferromagnetism, International Series of Monographs on Physics, Vol. 93, Oxford Science Publications, 1996.

[36] Skomski R., Oepen H.-P., Kirschner J., Phys. Rev. B 58 (1998) 3223.
[37] Brune H., Surf. Sci. Rep. 31 (1998) 121.
[38] Evans J.W., Bartelt M.C., Phys. Rev. B 63 (2001) 235408.
[39] Rusponi S., Cren T., Weiss N., Epple M., Buluschek P., Claude L., Brune H., Nat. Mater. 2 (2003) 546.
[40] Chantrell R.W., Ayoub N.Y., Popplewell J., J. Magn. Magn. Mater. 53 (1985) 199.
[41] Fruchart O., Jubert P.O., Meyer C., Klaua M., Barthel J., Kirschner J., J. Magn. Magn. Mater. 239 (2002) 224.
[42] Koide T., Miyauchi H., Okamoto J., Shidara T., Fujimori A., Fukutani H., Amemiya K., Takeshita H., Yuasa S., Katayama T., Suzuki Y., Phys. Rev. Lett. 87 (2001) 257201.
[43] Wu R., Li C., Freeman A.J., J. Magn. Magn. Mater. 99 (1991) 71.
[44] Nakajima N., Koide T., Shidara T., Miyauchi H., Fukutani H., Fujimori A., Iio K., Katayama T., Nyvlt M., Suzuki Y., Phys. Rev. Lett. 81 (1998) 5229.
[45] Ferrer S., Alvarez J., Lundgren E., Torrelles X., Fajardo P., Boscherini F., Phys. Rev. B 56 (1997) 9848.
[46] Gambardella P., Rusponi S., Veronese M., Dhesi S.S., Grazioli C., Dallmeyer A., Cabria I., Zeller R., Dederichs P.H., Kern K., Carbone C., Brune H., Science 300 (2003) 1130.
[47] Pick C., Stepanyuk V.S., Baranov A.N., Hergert W., Bruno P., Phys. Rev. B 68 (2003) 104410.
[48] Dürr H.A., Dhesi S.S., Dudzik E., Knabben D., Laan G.v.d., Goedkoop J.B., Hillebrecht F.U., Phys. Rev. B 59 (1999) R701.
[49] Zhang R., Willis R., Phys. Rev. Lett. 86 (2001) 2665.
[50] Frota-Pessôa S., Muniz R., Kudrnovsky J., Phys. Rev. B 62 (2000) 5293.
[51] Robach O., Quiros C., Steadman P., Peters K.F., Lundgren E., Alvarez J., Isern H., Ferrer S., Phys. Rev. B 65 (2002) 054423.
[52] Chantrell R.W., Walmsley N., Gore J., Maylin M., Phys. Rev. B 63 (2001) 024410.
[53] Haginoya C., Heike S., Ishibashi M., Nakamura K., Koike K., Yoshimura T., Yamamoto Y., Hirayama Y., J. Appl. Phys. 85 (1999) 8327.
[54] Sharrock M.P., IEEE Trans. Mag. 26 (1990) 193.
[55] We used the OOMMF program, release 1.1 beta 2 (http://math.nist.gov/oommf/).
[56] Schilfgaarde M.v., Antropov V.P., J. Appl. Phys. 85 (1999) 4827.
[57] Etzkorn M., Anil Kumar P.S., Tang W., Zhang Y., Kirschner J., Phys. Rev. B 72 (2005) 184420.
[58] Cren T., Rusponi S., Weiss N., Epple M., Brune H., J. Phys. Chem. B 108 (2004) 14685.
[59] Gambardella P., Dallmeyer A., Maiti K., Malagoli M., Eberhardt W., Kern K., Carbone C., Nature 416 (2002) 301.
[60] Hill T., Mozaffari-Afshar M., Schmidt J., Risse T., Freund H.J., Surf. Sci. 429 (1999) 246.
[61] Skumryev V., Stoyanov S., Zhang Y., Hadjipanayis G., Givord D., Nogués J., Nature 423 (2003) 850.
[62] Gambardella P., Šljivančanin Ž., Hammer B., Blanc M., Khunke K., Kern K., Phys. Rev. Lett 87 (2001) 056103.
[63] Petit C., Taleb A., Pileni M.P., J. Phys. Chem. B 103 (1999) 1805.
[64] Albrecht M., Hu G., Guhr I.L., Ulbrich T.C., Boneberg J., Leiderer P., Schatz G., Nat. Mater. 4 (2005) 203.
[65] Boneberg J., Burmeister F., Schafle C., Leiderer P., Reim D., Fery A., Herminghaus S., Langmuir 13 (1997) 7080.
[66] Barth J.V., Brune H., Ertl G., Behm R.J., Phys. Rev. B 42 (1990) 9307.
[67] Brune H., Kern K., in: Growth and Properties of Ultrathin Epitaxial Layers, D.A. King, D.P. Woodruff (eds.), Vol. 8 of The Chemical Physics of Solid Surfaces and Heterogeneous Catalysis, Elsevier Science, Amsterdam, 1997, p. 149.
[68] Brune H., Röder H., Boragno C., Kern K., Phys. Rev. B 49 (1994) 2997.

[69] Günther C., Vrijmoeth J., Hwang R.Q., Behm R.J., Phys. Rev. Lett. 74 (1995) 754.
[70] Brune H., Bromann K., Röder H., Kern K., Jacobsen J., Stoltze P., Jacobsen K., Nørskov J., Phys. Rev. B 52 (1995) R14380.
[71] Meyer J.A., Schmid P., Behm R.J., Phys. Rev. Lett. 74 (1995) 3864.
[72] Fischer B., Brune H., Fricke A., Barth J.V., Kern K., Phys. Rev. Lett. 82 (1999) 1732.
[73] Michely T., Hohage M., Esch S., Comsa G., Surf. Sci. 349 (1996) L89.
[74] Meyer J.A., Baikie J.D., Kopatzki E., Behm R.J., Surf. Sci. 365 (1996) L647.
[75] Takeshita H., Suzuki Y., Akinaga H., Mizutani W., Ando K., Katayama T., Itoh A., Tanaka K., J. Magn. Magn. Mater. 165 (1997) 38.
[76] Padovani S., Chado I., Scheurer F., Bucher J.P., Phys. Rev. B. 59 (1999) 11887.
[77] Chambliss D.D., Wilson R.J., Chiang S., Phys. Rev. Lett. 66 (1991) 1721.
[78] Voigtländer B., Meyer G., Amer N.M., Phys. Rev. B 44 (1991) 10354.
[79] Padovani S., Molinàs-Mata P., Scheurer F., Bucher J.P., Appl. Phys. A 66 (1998) 1199.
[80] Voigtländer B., Meyer G., Amer N.M., Surf. Sci. 255 (1991) L529.
[81] Stroscio J.A., Pierce D.T., Dragoset R.A., First P.N., J. Vac. Sci. Technol. A 10 (1992) 1981.
[82] Altman E.I., Colton R.J., Surf. Sci. 304 (1994) L400.
[83] Chambliss D.D., Wilson R.J., J. Vac. Sci. Technol. B 9 (1991) 928.
[84] Krzyzowski M.A., Ph.D. thesis, Bonn, 1995.
[85] Fischer B., Barth J.V., Fricke A., Nedelmann L., Kern K., Surf. Sci. 389 (1997) 366.
[86] N'Diaye A., Bleikamp S., Feibelman P.J., Michely T., Phys. Rev. Lett. 97 (2006) 215501.
[87] Bromann K., Giovannini M., Brune H., Kern K., Eur. Phys. J. D 9 (1999) 25.
[88] Giovannini M., Metallic Thin Layers and Nanostructures: Fabrication and Characterization, Ph.D. thesis, EPFL, 2000.
[89] Holst B., Hohlen M., Wandelt K., Allison W., Surf. Sci. 377–379 (1997) 891.
[90] Pedersen M.Ø., Bönicke I.A., Lægsgaard E., Stensgaard I., Ruban A., Nørskov J.K., Besenbacher F., Surf. Sci. 387 (1997) 86.
[91] Figuera J.d.l., Prieto J.E., Ocal C., Miranda R., Phys. Rev. B 47 (1993) 13043.
[92] Figuera J.d.a., Prieto J.E., Kostka G., Müller S., Ocal C., Miranda R., Heinz K., Surf. Sci. 349 (1996) L139.
[93] Rabe A., Memmel N., Steltenpohl A., Fauster T., Phys. Rev. Lett. 73 (1994) 2728.
[94] Diekhöner L., Schneider M.A., Baranov A.N., Stepanyuk V.S., Bruno P., Kern K., Phys. Rev. Lett. 90 (2003) 236801.
[95] Pietzsch O., Kubetzka A., Bode M., Wiesendanger R., Phys. Rev. Lett. 92 (2004) 057202.
[96] Repain V., Baudot G., Ellmer H., Rousset S., Europhys. Lett. 58 (2002) 730.
[97] Repain V., Baudot G., Ellmer H., Rousset S., Mater. Sci. Eng. B 96 (2002) 178.
[98] Rohart S., Baudot G., Repain V., Girard Y., Rousset S., Bulou H., Goyhenex C., Proville L., Surf. Sci. 559 (2004) 47.
[99] Brune H., in: Properties of Single Organic Molecules on Crystal Surfaces, F. Rosei, P. Grütter, W. Hofer (eds.), Springer, New York, 2006, p. 247.
[100] Besenbacher F., Nielsen L.P., Sprunger P.T., in: Growth and Properties of Ultrathin Epitaxial Layers, D.A. King, D.P. Woodruff (eds), Vol. 8 of The Chemical Physics of Solid Surfaces and Heterogeneous Catalysis, Elsevier Science, Amsterdam, 1997, p. 207.
[101] Böhringer M., Jiang Q., Berndt R., Schneider W.D., Zegenhagen J., Surf. Sci. 367 (1996) 245.
[102] Wiederholt T., Brune H., Wintterlin J., Behm R.J., Ertl G., Surf. Sci. 324 (1995) 91.
[103] Degen S., Krupski A., Kralj M., Langner A., Becker C., Sokolowski M., Wandelt K., Surf. Sci. 576 (2005) L57.
[104] Corso M., Auwärter W., Muntwiler M., Tamai A., Greber T., Osterwalder J., Science 303 (2004) 217.
[105] Becker C., Rosenhahn A., Wiltner A., Bergmann K.v., Schneider J., Pervan P., Milun M., Kralj M., Wandelt K., New J. Phys. 4 (2002) 75.

[106] Degen S., Becker C., Wandelt K., Faraday Discuss 125 (2004) 343.
[107] Lehnert A., Krupski A., Degen S., Franke K., Decker R., Rusponi S., Kralj M., Becker C., Brune H., Wandelt K., Surf. Sci. 600 (2006) 1804.
[108] Weaver J.H., Waddill G.D., Science 251 (1991) 1444.
[109] Vandoni G., Félix C., Monot R., Buttet J., Harbich W., Chem. Phys. Lett. 229 (1994) 51.
[110] Bromann K., Félix C., Brune H., Harbich W., Monot R., Buttet J., Kern K., Science 274 (1996) 956.
[111] Thole B., Carra P., Sette F., van der Laan G., Phys. Rev. Lett. 68 (1992) 1943.
[112] Carra P., Thole B., Altarelli M., Wang X., Phys. Rev. Lett. 70 (1993) 694.
[113] Gambardella P., Dallmeyer A., Maiti K., Malagoli M., Rusponi S., Ohresser P., Eberhardt W., Carbone C., Kern K., Phys. Rev. Lett. 93 (2004) 077203.
[114] Ohresser P., Brookes N.B., Padovani S., Scheurer F., Bulou H., Phys. Rev. B 64 (2001) 104429.
[115] Chen C., Ydzerda Y., Lin H.-J., Smith N.V., Meigs G., Chaban E., Ho G.H., Pellegrin E., Sette F., Phys. Rev. Lett. 75 (1995) 152.
[116] Bruno P., Phys. Rev. B 39 (1989) 865.
[117] Weller D., Stöhr J., Nakajima R., Carl A., Samant M.G., Chappert C., Mégy R., Beauvillain P., Veillet P., Held G.A., Phys. Rev. Lett. 75 (1995) 3752.
[118] Stöhr J., J. Magn. Magn. Mater. 200 (1999) 470.
[119] Fruchart O., Klaua M., Barthel J., Kirschner J., Phys. Rev. Lett. 83 (1999) 2769.
[120] Nonas B., Cabria I., Zeller R., Dederichs P.H., Huhne T., Ebert H., Phys. Rev. Lett. 86 (2001) 2146.
[121] Félix-Medina R., Guirado-López R., Dorantes-Dávila J., Pastor G.M., J. Appl. Phys. 87 (2000) 4894.
[122] Wildberger K., Stepanyuk V.S., Lang P., Zeller R., Dederichs P.H., Phys. Rev. Lett. 75 (1995) 509.
[123] Billas I.M.L., Châtelain A., Heer W.A.d., Science 265 (1994) 1682.
[124] Apsel S.E., Emmert J.W., Deng J., Bloomfield L.A., Phys. Rev. Lett. 76 (1996) 1441.
[125] Weller D., Moser A., IEEE Trans. Mag. 35 (1999) 4423.
[126] van der Laan G., J. Phys.: Condens. Matter 10 (1998) 3239.
[127] Lazarovits B., Szunyogh L., Weinberger P., Phys. Rev. B 67 (2003) 024415.
[128] Solovyev I.V., Dederichs P.H., Mertig I., Phys. Rev. B 52 (1995) 13419.
[129] Mishra A., Wernsdorfer W., Abboud K.A., Christou G., J. Am. Chem. Soc. 126 (2004) 15648.
[130] Hirjibehedin C.F., Lutz C.P., Heinrich A.J., Science 312 (2006) 1021.
[131] Gambardella P., Dhesi S.S., Gardonio S., Grazioli C., Ohresser P., Carbone C., Phys. Rev. Lett. 88 (2002) 047202.
[132] van der Laan G., Thole B.T., Phys. Rev. B 43 (1991) 13401.
[133] van der Laan G., Thole B.T., Phys. Rev. B 42 (1990) 6670.
[134] Gallagher W.J., Parkin S.P., IBM J. Res. Dev. 50 (2006) 5.
[135] Parkin S.S.P., Xin J., Kaiser C., Panchula A., Roche K., Samant M., IEEE Proc 91 (2003) 661.
[136] Moodera J.S., Kinder L.R., Wong T.M., Meservey R., Phys. Rev. Lett. 74 (1995) 3273.
[137] Miyazaki T., Tezuka N., J. Magn. Magn. Mater. 139 (1995) L231.
[138] Butler W.H., Zhang X.-G., Schulthess T.C., MacLaren J.M., Phys. Rev. B 63 (2001) 054416.
[139] Mathon J., Umerski A., Phys. Rev. B 63 (2001) 220403.
[140] Parkin S.S.P., Kaiser C., Panchula A., Rice P.M., Hughes B., Samant M., Yang S.H., Nat. Mater. 3 (2004) 862–867.
[141] Yuasa S., Fukushima A., Kubota H., Suzuki Y., Ando K., Appl. Phys. Lett. 89 (2006) 042505.

[142] Wiesendanger R., Bode M., Getzlaff M., Appl. Phys. Lett. 75 (1999) 124.
[143] Rusponi S., Weiss N., Cren T., Epple M., Brune H., Appl. Phys. Lett. 87 (2005) 162514.
[144] Grütter P., Dürig U.T., Phys. Rev. B 49 (1994) 2021.
[145] Lundgren E., Stanka B., Schmid M., Varga P., Phys. Rev. B 62 (2000) 2843.
[146] Kubetzka A., Bode M., Pietzsch O., Wiesendanger R., Phys. Rev. Lett. 88 (2002) 057201.
[147] Brune H., e-J. Surf. Sci. Nanotechnol. 4 (2006) 478.
[148] Ding H.F., Wulfhekel W., Henk J., Bruno P., Kirschner J., Phys. Rev. Lett. 90 (2003) 116603.
[149] Soulen R.J., Jr., Byers J.M., Osofsky M.S., Nadgorny B., Ambrose T., Cheng S.F., Broussard P.R., Tanaka C.T., Nowak J., Moodera J.S., Barry A., Coey J.M.D., Science 282 (1998) 85.
[150] Upadhyay S.K., Palanisami A., Louie R.N., Buhrman R.A., Phys. Rev. Lett. 81 (1998) 3247.
[151] Niebergall L., Stepanyuk V.S., Berakdar J., Bruno P., Phys. Rev. Lett. 96 (2006) 127204.
[152] Pietzsch O., Okatov S., Kubetzka A., Bode M., Heinze S., Lichtenstein A., Wiesendanger R., Phys. Rev. Lett. 96 (2006) 237203.
[153] Rau C., Eichner S., Phys. Rev. Lett. 47 (1981) 939.